

EFFECTS OF HYDROGEN ON THE FRACTURE TOUGHNESS OF 42CrMo4 STEEL QUENCHED AND TEMPERED AT DIFFERENT TEMPERATURES

A. Zafra^{1*}, L.B. Peral*, J. Belzunce* and C. Rodríguez*

¹Corresponding author: Alfredo Zafra García (+34 985182023) alfredyzafr@gmail.com

*University of Oviedo, campus universitario, Edificio de Energía, 33203, Gijón, Spain

ABSTRACT

The aim of this paper is to study the effect of hydrogen on the fracture toughness of 42CrMo4 steel quenched and tempered at 500, 550, 600, 650 and 700°C. The influence of hydrogen was assessed by means of fracture toughness tests carried out on compact CT specimens, pre-charged with gaseous hydrogen in a pressurized reactor at 19.5MPa and 450°C for 21h. Thermal desorption analysis (TDA) and finite element simulations (FEM) were employed to study the hydrogen diffusivity and solubility of the different steel grades. Additionally, X-ray diffraction (XRD) was used to determine the dislocation densities present in these steel microstructures and scanning electron microscopy (SEM) to analyse them and to identify the fracture micromechanisms that took place during the fracture toughness tests.

According to the obtained results, dislocation density, hydrogen solubility and residual hydrogen strongly trapped in the steel microstructure were seen to decrease with increasing tempering temperature, following the apparent hydrogen diffusion coefficient the opposite trend. It was also observed that hydrogen embrittlement was much greater in the steel grades tempered at the lowest temperatures (with higher yield strength), and in tests performed at the lowest displacement rates. Moreover, a change in the fracture micromechanism was detected, from ductile (microvoids coalescence, MVC) in the absence of hydrogen, to intermediate (plasticity-related hydrogen induced cracking, PRHIC) in the case of the hydrogen pre-charged steels with relatively low yield strengths under low displacement rates and, finally, to a fully brittle behaviour (mostly intergranular fracture, IG) in the case of steels with the highest strengths, tested at low displacement rates.

It was finally demonstrated that only diffusible hydrogen, hydrogen atoms able to move at room temperature, is responsible for hydrogen embrittlement.

KEYWORDS: Hydrogen embrittlement, fracture toughness, 42CrMo4, hydrogen diffusion, quench and tempering treatments, failure micromechanisms.

1. INTRODUCTION

The emerging need to replace fossil fuels in favour of cleaner and renewable alternatives is boosting the development of hydrogen-based energy applications, such as fuel cells. In this context, the increasing demand of hydrogen in the years to come means that traditional systems and materials, previously used for hydrogen transport and storage, should be adapted to allow delivering larger hydrogen quantities in a more efficient way. Furthermore, due to the low energy density of hydrogen, transport and storage units (pipes and vessels) will be designed to sustain higher hydrogen pressures, up to 100 MPa. Under these hydrogen high pressures, hydrogen enters into the containing structural materials and hydrogen embrittlement phenomena (HE) can take place.

Typically, hydrogen facilities have been designed using metallic materials with high resistance to hydrogen embrittlement, such as austenitic stainless steel or aluminium alloys. However, such metallic alloys have lower strength and are more expensive than conventional steels, such as carbon and low-alloy steels [1]. Then, the best economical solution to manufacture hydrogen facilities would be the use of medium and high-strength steels in order to reduce the thickness of pipes and vessels and so the material costs.

42CrMo4 steel belongs to the family of Cr-Mo steels, which are frequently used in the quenched and tempered condition when a good combination of strength and toughness is required. This family of steels also has high fatigue strength, making it an excellent choice for the manufacture of vessels and pipes able to work under high-pressure hydrogen gas [2, 3]. Nevertheless, it is well known that medium-high strength steels are more sensitive to hydrogen embrittlement than low-strength steels, and this susceptibility increases with the strength level of the steel [4, 5]. In

order to solve this drawback, they may be tempered at high temperatures, where their strength and hardness significantly decline as was shown in [6], where the application of tempering temperatures of 650° and 700°C during two hours gave rise to the best notched tensile behaviour under internal hydrogen. Tvrđy et al. [7] studied the hydrogen embrittlement of CrMo and CrMoV pressure vessel steels and demonstrated that even low and medium-strength pressure vessel steels are susceptible to hydrogen embrittlement and to subcritical crack growth under stress intensity factor levels far beneath the relevant critical fracture toughness value, K_{IC} . They further proved that the resistance to hydrogen embrittlement strongly depends on the applied heat treatment, on the resultant microstructure (carbide precipitation and distribution) and on the strength level attained, obtaining the best resistance to hydrogen embrittlement with steels tempered at the maximum available temperature. Additionally, during welding processes of pipes and vessels, these steel grades suffer local hardening due to martensitic/bainitic transformation and, thus, the possibility of cold cracking due to the presence of hydrogen significantly increases, making necessary the application of post-welding heat treatments (PWHT). In fact, Mitchell et al. [8] studied the optimisation of PWHT in a 1.25Cr-0.5Mo pressure vessel steel for high temperature hydrogen service and suggested that a tempering stage in the range of 670°-710°C for 8 hours represented the optimal solution for resistance to hydrogen embrittlement.

Many researchers have studied the effect of hydrogen on the tensile properties of medium-and high-strength ferritic steels, reporting that hydrogen embrittlement not only depends on the strength level of the steel, which is directly related to its microstructure [9], but also on other factors such as the way hydrogen is charged into the specimen (gas charge or electrochemical charge) [10]; the dimensions and geometry of the component, for example the presence of notches or cracks [11, 12]; and also on certain testing parameters, such as the applied strain rate [13-15]. All these aspects related to hydrogen embrittlement of 42CrMo4 steel quenched and tempered at different temperatures were already considered in a previous work [6].

Furthermore, the effect of hydrogen on the fatigue crack growth of quenched and tempered steels has also been widely studied [16-20], pointing out the influence of the applied ΔK factor and test frequency in the hydrogen embrittlement phenomenon. Even some works, have focused on the fatigue behaviour of the 42CrMo4 steel itself, under high pressure hydrogen gas [21], introducing hydrogen by cathodic charging [22] and also pre-charging the specimens in high temperature, high pressure hydrogen gas [23].

Regarding fracture toughness properties, it is worth noting the work carried out by Splichal et al. [24], who evaluated the effects of hydrogen on the static fracture toughness using cathodically charged specimens of Eurofer 97 steel, reporting that an increase in hydrogen content resulted in a drastic drop of the fracture toughness for the onset of crack growth parameter, $J_{0.2}$, and in a noticeable change of the fracture micromechanism, from a ductile to a wholly brittle one. Ogawa et al. [25] performed room temperature fracture toughness tests on compact tensile (CT) specimens on a low carbon steel (with a yield strength of 360 MPa), both in air and in hydrogen gas under pressures of 0.7 and 115 MPa, noticing a significant degradation in the fracture toughness properties, visible in the load-displacement plots and also in the toughness-crack growth curves. The behaviour of the specimen tested under the highest hydrogen pressure (with more internal hydrogen content) was the most affected by hydrogen embrittlement, giving rise to a fracture surface covered by quasi cleavage (QC) facets. Similarly, Liu et al. [26] observed a drop in the fracture toughness of a ferritic SA508-III steel as the hydrogen content introduced in the steel increased, also changing the fracture pattern from a ductile microvoid coalescence fracture micromechanism to a mixture of dimples and cleavage facets.

However, the influence of hydrogen on the fracture toughness of ferritic-martensitic steels still needs additional studies, to attain a better comprehension of the effects that heat treatment, microstructure, strength level, hydrogen diffusion and hydrogen content have on the fracture toughness of the steel. Additionally, the modification of fracture micromechanisms by the presence of internal or external hydrogen, although already studied in several works [27-29], is sometimes still controversial and need deeper studies.

In this context, the main objective of this work is to analyse the influence of strength level and microstructure (influence of applying different tempering temperatures onto a previously quenched 42CrMo4 steel) in the hydrogen embrittlement susceptibility of the steel, assessed through fracture toughness tests performed on hydrogen gas pre-charged CT specimens. Additionally, the ability of the steel to recover its original properties when specimens were left in air at room temperature during certain periods of time was also evaluated.

2. EXPERIMENTAL PROCEDURE

2.1 Material and heat treatments

A 42CrMo4 steel was used in the present study. Its chemical composition in weight % is shown in Table 1.

Steel	C	Cr	Mo	Mn	Si	P	S
42CrMo4	0.42	0.98	0.22	0.62	0.18	0.008	0.002

Table 1. Chemical composition of 42CrMo4 steel (wt. %).

Hot rolled plates (with a thickness of 12 mm) of 42CrMo4 were austenitized at 845°C for 40 min, quenched in water, and then tempered at 5 different temperatures between 500 and 700°C, for 2 hours. The reason for using different heat treatments was to obtain different steel grades in order to analyse the way hydrogen degrades the fracture toughness of the same steel but with different microstructures and strength levels. The sequence of heat treatments and the nomenclature of the 42CrMo4 steel grades are shown in Table 2.

Specimen ID	Heat treatments
42CrMo4_700	845°C/40min + water quenching + 700°C/2h tempering
42CrMo4_650	845°C/40min + water quenching + 650°C/2h tempering
42CrMo4_600	845°C/40min + water quenching + 600°C/2h tempering
42CrMo4_550	845°C/40min + water quenching + 550°C/2h tempering
42CrMo4_500	845°C/40min + water quenching + 500°C/2h tempering

Table 2. Heat treatments applied to the 42CrMo4 steel.

2.2 Dislocation density estimation

The dislocation density present in the 42CrMo4 steel grades was experimentally determined by means of X-ray diffraction. Diffraction peaks corresponding to {110}, {220} and {211} planes were recorded in order to determine their diffraction peak widths at half maximum, β (FWHM). The obtained data were analyzed using the Williamson-Hall Equation (1) [29, 30]:

$$\beta \frac{\cos(\theta)}{\lambda} = \frac{0.9}{d} + 2\varepsilon \frac{\sin(\theta)}{\lambda} \quad (1)$$

being θ the diffraction angle related to each crystallographic plane (69°, 106.1° and 156.4°), λ the X-ray wavelength (0.229 nm for a chromium tube), d the crystallite size, and ε the local strain. The slope of the straight line, which is obtained by plotting the left term of equation (1) against $\sin\theta/\lambda$, gives ε . The dislocation density, ρ , was finally obtained by means of Equation (2), taking also into account the characteristic Burgers vector of the ferritic matrix, $b=0.248\text{nm}$ [31]:

$$\rho = 14.4 \left(\varepsilon/b \right)^2 \quad (2)$$

2.3 Hydrogen pre-charge

All the specimens were pre-charged with gaseous hydrogen in a high-pressure hydrogen reactor. In order to ensure that all the specimens were saturated with hydrogen (the maximum thickness of specimens was 10 mm), the following conditions were applied: 21 hours at 450°C under a pressure of 19.5 MPa of pure hydrogen.

The high temperature hydrogen solubility of the quenched and tempered 42CrMo4 steel grades under high pressure hydrogen can be approximated by the lattice hydrogen content of BCC iron, as reported by Hirtz [32], using Equation (3), and considering that traps are not active at this high temperature:

$$C_H = 104.47 \cdot \sqrt{f} \cdot e^{(-28600/RT)} \quad (3)$$

where f represents the fugacity in MPa. According to San Marchi [33], fugacity can be expressed from the hydrogen pressure, p , according to Equation (4):

$$f = p \cdot e^{(bp/RT)} \quad (4)$$

being b a constant of value 15.84, and the pressure, p , is expressed in MPa. Applying these equations to our hydrogen charging conditions, a hydrogen content of 4.1 ppm was introduced into the samples of the 42CrMo4 steel.

After the 21 hours of maintenance of the specimens in the hydrogen reactor, a cooling phase of 1h, until reaching a temperature of 85°C was always necessary to allow specimens to be removed from the reactor. Although hydrogen pressure was maintained during cooling, the decrease in temperature creates a thermodynamic driving force for hydrogen egress from the specimens, leading to a significant hydrogen loss in all cases. The hydrogen pre-charged specimens were then removed from the reactor and rapidly immersed in liquid nitrogen (-196°C), where they were kept until the moment of testing, in order to avoid additional hydrogen losses.

2.4 Measurement of hydrogen content

The hydrogen content in the specimens was measured by means of thermal desorption analysis (TDA), using a LECO DH603 hydrogen analyser. The equipment's measurement principle is based on the difference in thermal conductivity between a reference gas flow of pure nitrogen and a secondary flow composed of nitrogen and the hydrogen thermally extracted from the analysed specimen.

As one of the purposes of this study was to correlate the loss of toughness properties with the amount of hydrogen present in the steel during the tests, the hydrogen desorption curves of the different steel grades were determined at room temperature. These curves represent the hydrogen content versus time elapsed at room temperature (ppm vs time). Hydrogen pre-charged cylindrical pins with a diameter of 10 mm and a length of 30 mm long (≈ 20 g) were used to obtain the steel desorption curves.

The procedure to obtain the desorption curves was the following. All the hydrogen pre-charged pins were removed from the liquid nitrogen at the same time and left in air at RT. Then, the hydrogen concentration of the different samples was measured at different time intervals. Before starting the measurement, each pin was cleaned in an ultrasonic bath with acetone for 5 minutes and carefully dried using cold air. The analysis to determine the hydrogen concentration consisted in keeping the sample at 1100°C for 400 s.

2.5 Determination the hydrogen diffusion coefficient at room temperature

Numerical fitting of the experimentally measured hydrogen desorption data was used to estimate the apparent hydrogen diffusion coefficient (D_{app}) of the five steel grades. An axisymmetric bi-dimensional diffusion analysis of the aforementioned cylindrical samples was performed using a commercial FEM software (Abaqus Cae) employing 4 node linear axisymmetric quadrilateral elements. The initial hydrogen content experimentally determined at the end of the cooling phase (from 450 to 85°C in the high pressure reactor) by means of the LECO analyser was taken as the first point of the analysis (boundary condition 1). The residual hydrogen content, likewise determined using the LECO analyser after a long stay at room temperature (about one month), was taken as our surface condition, residual hydrogen (boundary condition 2).

Fick's diffusion law, described in Equation (5), was applied to a cylinder with a radius (R) of 5 mm. J being the hydrogen flux, D_{app} the apparent diffusion coefficient, and C_H representing the hydrogen concentration in the specimen.

$$J = -D_{app} \nabla C_H \quad (5)$$

By varying the apparent diffusion coefficient, D_{app} , the hydrogen evolution over time at room temperature was calculated (only radial diffusion was considered). The diffusion coefficient which best fitted the experimental data was taken as the apparent diffusion coefficient of the steel.

2.6 Fracture toughness tests

Fracture toughness characterization was performed using compact tensile (CT) specimens with a width, $W=48$ mm, a thickness, $B=12$ mm, and an initial notch $a_0=20$ mm. First, the specimens were fatigue pre-cracked at $R=0.1$ and $f=10$ Hz, up to obtaining a crack length versus width ratio, $a/W=0.5$, following the ASTM E1820 standard [34]. Afterwards, lateral notches were machined on both sides of the specimen until reaching a net thickness, $B_n=10$ mm, as to assure a plane strain state.

Fracture toughness tests without hydrogen were carried out under a nominal displacement rate of 1 mm/min for steel grades tempered at 700, 650 and 600°C, and a rate of 0.1 mm/min was used for the steel grades tempered at lower temperatures. Hydrogen pre-charged specimens were tested under displacement rates of 1, 0.1, 0.01 and 0.001mm/min (also depending on the steel grade) to study the influence of this parameter on HE. Additionally, in order to evaluate the ability of the steel to recover its mechanical properties as hydrogen progressively egress from the specimens, hydrogen pre-charged CT specimens were degassed in air at room temperature for different times and then tested at the same displacement rate to determine the fracture toughness.

Crack growth in the course of tests was determined by means of the compliance method, and 25% partial discharges were carried out using a COD gauge. The initial and final crack lengths were corrected by measuring them on the fracture surface of the broken specimen. The value of J obtained in each discharge was calculated as the sum of its elastic and plastic component. The former was calculated from the stress intensity factor, K , and the latter was obtained by integrating the area below the load-LLD (load line displacement) plot, always following the procedure described in the ASTM E1820 standard [34].

The $J_{0.2/BL}$ (kJ/m²) parameter was employed to assess the fracture toughness for the onset of crack growth. This parameter corresponds to the value of J after a crack growth of 0.2 mm regarding the blunting of the crack tip.

It should be noted that, due to the high brittleness of the steel grades tempered at 550 and 500°C and tested with internal hydrogen under low displacement rates, it was not possible to determine the value of $J_{0.2/BL}$. Therefore, for these steel grades, the value of P_Q was calculated from the load-COD curve, being P_Q the maximum load, load at instability, and from this value, the K_Q and J_Q parameters were estimated following the indications of the aforementioned standard [34].

Finally, the decay of fracture toughness caused by the presence of hydrogen was defined by means of the embrittlement index (EI), defined in Equation 6 (EI varies from 0, no embrittlement at all, to 100%, maximum possible hydrogen embrittlement).

$$EI(X)[\%] = \frac{X - X_H}{X} \cdot 100 \quad (6)$$

where X and X_H are the measured toughness property respectively evaluated without and with hydrogen.

2.7 Observation of microstructures and fracture surfaces

The microstructures obtained after the application of the different heat treatments were observed by means of a scanning electron microscope (SEM JEOL-JSM5600) under an acceleration voltage of 20 kV. The samples were ground, polished with diamond paste, and finally etched with Nital-2%.

The fracture surfaces of the tested specimens were also analysed using the same scanning electron microscope under different magnifications.

3. RESULTS

3.1 Steel microstructures

The SEM microstructures of the five grades of 42CrMo steel are shown in Figure 1 under a magnification of 10,000x.

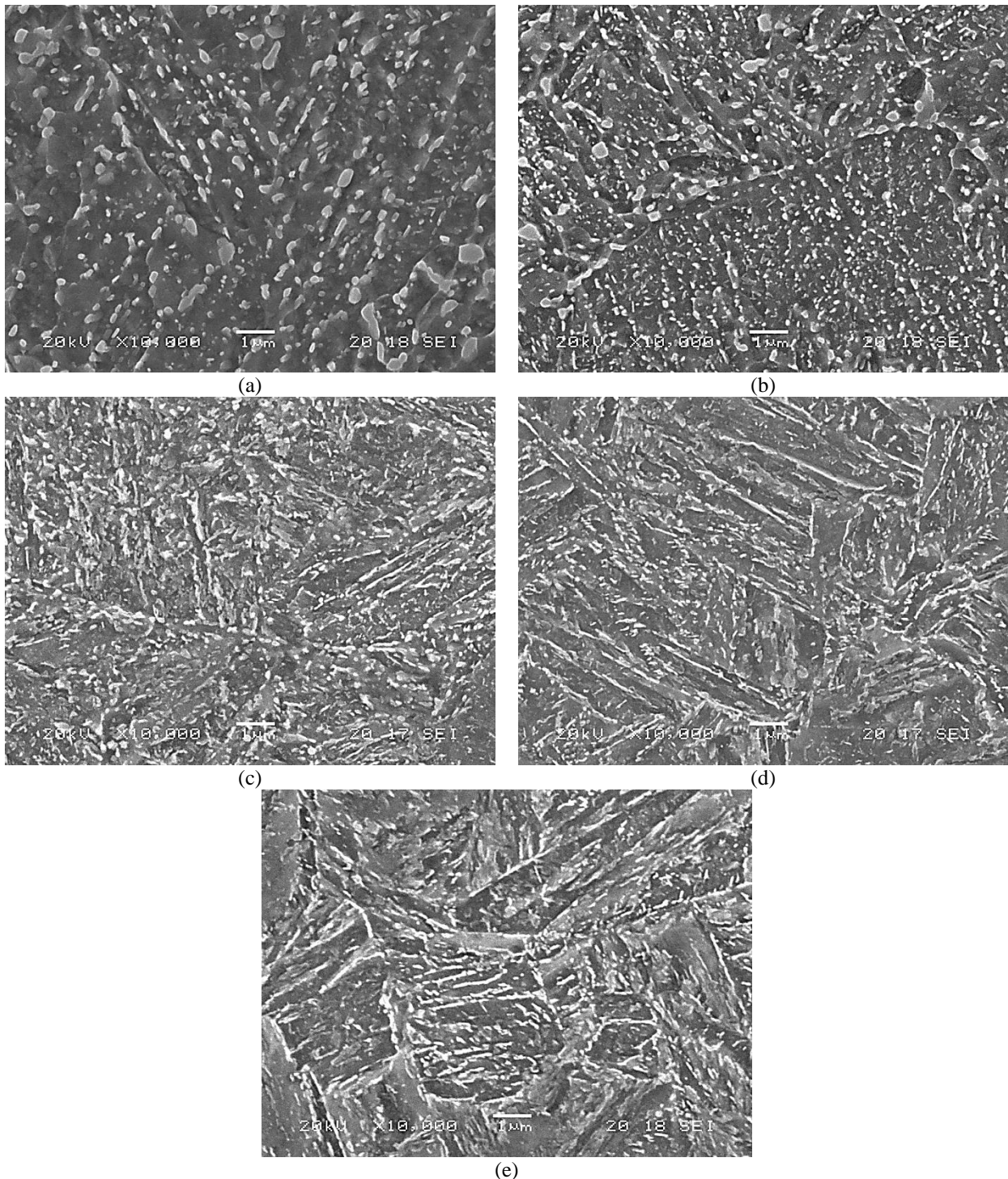


Figure 1. SEM microstructures of 42CrMo4 steel quenched and tempered (2h) at (a) 700°C, (b) 650°C, (c) 600°C, (d) 550°C and (e) 500°C (10,000x).

The microstructure of all the 42CrMo4 grades was tempered martensite (the profuse carbide precipitation that takes place during the tempering stage is clearly seen). Microstructure acicularity decreases, internal residual stresses are released and the extension of martensite lath boundaries decreases with increasing tempering temperature [35]. Furthermore, elongated carbides break up, globulize, and finally grow to yield a more uniform distribution.

The aforementioned microstructural differences give rise to the hardness and tensile properties listed in Table 3 [6]. As expected, yield strength, σ_{ys} , ultimate tensile strength, σ_{uts} and Brinell hardness, HB, progressively decrease with increasing tempering temperature, while the opposite occurs with tensile elongation, e, and reduction in area, RA. Additionally, Table 3 shows the dislocation density obtained using X-ray diffraction and the Williamson-Hall approach, equations (1) and (2). Dislocation density increases as tempering temperature decreases, as expected.

Steel Grades	Heat treatment	σ_{ys} [MPa]	σ_{uts} [MPa]	e [%]	RA [%]	HB	ρ [cm ⁻²]
42CrMo4_700	845°C+WQ+T700°C/2h	622	710	22.4	61.3	201	$6.5 \cdot 10^{11}$
42CrMo4_650	845°C+WQ+T650°C/2h	820	905	16.3	57.1	246	$7.5 \cdot 10^{11}$
42CrMo4_600	845°C+WQ+T600°C/2h	880	985	14.6	55.4	281	$8.0 \cdot 10^{11}$
42CrMo4_550	845°C+WQ+T550°C/2h	1023	1113	13.9	48.9	307	$9.9 \cdot 10^{11}$
42CrMo4_500	845°C+WQ+T500°C/2h	1086	1198	12.7	50.6	335	$1.1 \cdot 10^{12}$

Table 3. Tensile properties, hardness (HB) and dislocation density of the different 42CrMo4 grades.

It is well known that hydrogen embrittlement increases with the strength level of the steel [4-6], hence grades tempered at lower temperatures are expected to be more susceptible to HE.

3.2. Hydrogen desorption curves and diffusion coefficient estimation

The hydrogen desorption data experimentally obtained at room temperature for each steel grade are shown in Figure 2 along with the fitted FEM simulated curves. These figures represent the evolution of the hydrogen content (ppm) versus the exposure time in air (hours) at room temperature. Significant good fitting between the experimental data and the numerical simulation results was obtained with all the steel grades.

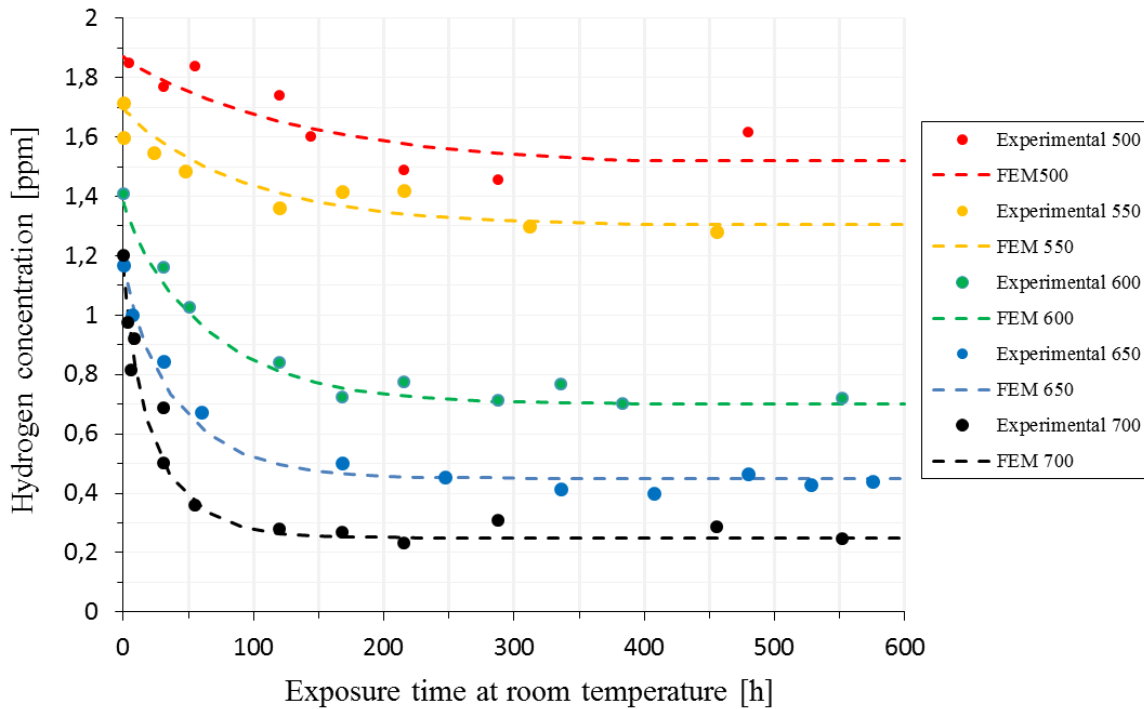


Figure 2. Hydrogen desorption curves. Experimental data (points) and numerical fitting (lines).

The initial hydrogen content, C_{H0} , corresponds to the first point of the desorption curve (hydrogen content at the end of the cooling phase following thermal pre-charging in the hydrogen reactor). The residual hydrogen, C_{Hr} , is the hydrogen strongly trapped in the steel microstructure, i.e. the hydrogen content after a long exposure at room temperature (in this case after nearly one month). The diffusible hydrogen, defined as the amount of hydrogen that is able to overcome traps and diffuse out of the steel when sufficient time is available, was calculated as the difference between the initial and residual hydrogen contents ($C_{H0} - C_{Hr}$).

As previously stated, data fitting of the experimentally measured hydrogen desorption results was used to estimate the apparent hydrogen diffusion coefficient, D_{app} , in the different steel grades. As an example, the homogeneous hydrogen concentration at the end of hydrogen pre-charging is shown in figure 3(a) and the initial hydrogen distribution at the end of the cooling phase (from 450 to 85°C performed in the high pressure reactor) in the case of the 42CrMo4_700 steel is also shown in Figure 3(b). This hydrogen distribution corresponds to the first data point of the desorption curve, where an average hydrogen content of 1.2 ppm was experimentally measured. However, at this moment the specimen surface retains the residual hydrogen content (0.3 ppm in this steel grade, which represents our surface boundary condition), but hydrogen contents as high as 2.2 ppm are still present in the centre of the specimen. Figure 3(c) corresponds to the final situation, after a sufficiently long hold time at room temperature, where all the sample has the residual hydrogen content (0.3 ppm in this steel grade). As already mentioned, the diffusion coefficient which provides the best fit to the experimental data was taken as the RT apparent diffusion coefficient of the steel. In this case, the D_{app} value estimated for the 42CrMo4_700 steel grade was $4.2 \cdot 10^{-10}$ m²/s.

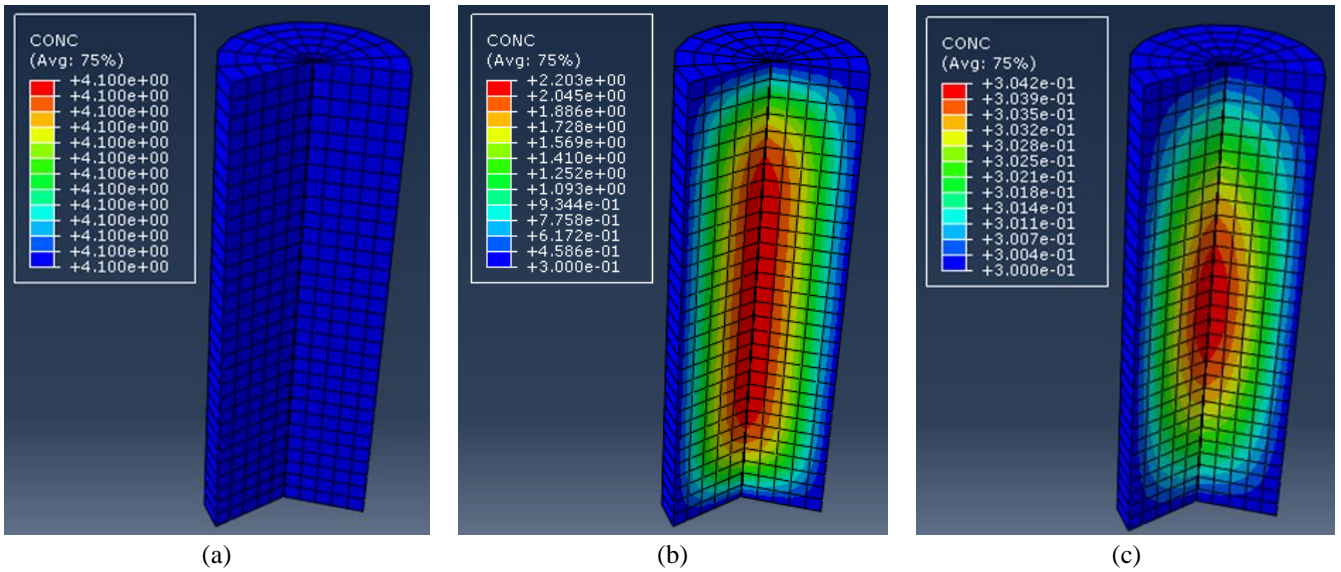


Figure 3. Hydrogen distribution in the 42CrMo4_700 steel in samples with $R=5$ mm and $L=30$ mm. (a) Homogeneous hydrogen concentration at the end of pre-charging (4.1 ppm). (b) Initial concentration (average hydrogen concentration of 1.2 ppm) measured on the LECO DH603 analyser at the end of the cooling phase. (c) Residual hydrogen concentration (average hydrogen concentration of 0.3 ppm) after 48h at RT.

The results obtained from the analysis of hydrogen desorption, for all the steel grades, are summarized in Table 4. A good correlation was obtained between the steel tempering temperature (or the steel hardness) with the different hydrogen contents and the apparent diffusion coefficient: As the steel tempering temperature decreases (hardness increases), initial and residual hydrogen significantly increase and apparent hydrogen diffusion coefficient decreases.

Steel Grades	HB	C_{H0} [ppm]	C_{Hr} [ppm]	$C_{H0}-C_{Hr}$ [ppm]	D_{app} [m ² /s]
42CrMo4_700	201	1.20	0.30	0.90	$4.2 \cdot 10^{-10}$
42CrMo4_650	246	1.20	0.45	0.75	$2.5 \cdot 10^{-10}$
42CrMo4_600	281	1.40	0.70	0.70	$1.5 \cdot 10^{-10}$
42CrMo4_550	307	1.70	1.30	0.40	$9.0 \cdot 10^{-11}$
42CrMo4_500	335	1.85	1.50	0.35	$6.6 \cdot 10^{-11}$

Table 4. Initial (C_{H0}), residual (C_{Hr}), diffusible hydrogen ($C_{H0}-C_{Hr}$) and apparent diffusion coefficient at room temperature, D_{app} , measured on the different 42CrMo4 steel grades.

3.2 Fracture toughness

3.2.1. Uncharged specimens

The fracture toughness results regarding the steel grades tested without hydrogen are shown in Figure 4 and Table 5. Figure 4 shows the load versus the load line displacement (LLD) curves and also the J-resistance curves, J parameter versus crack growth, J- Δa curves, derived from the former ones. The potential law from the fitted experimental data, $J=C_1\Delta a^{C_2}$, is also included in Table 5, allowing to estimate the J value for any value of crack growth. The J value for the onset of crack growth, $J_{0.2/BL}$, was also calculated. As expected, the value of $J_{0.2/BL}$ decreases as the tempering temperature decreases (higher yield strength and ultimate tensile strength), and also does the C_2 parameter, which means a flatter crack propagation curve. In all the cases, the operative fracture micromechanism was fully ductile, microvoids coalescence (MVC), as can be seen in Figure 5, for the specimens tempered at 700, 600 and 500°C respectively.

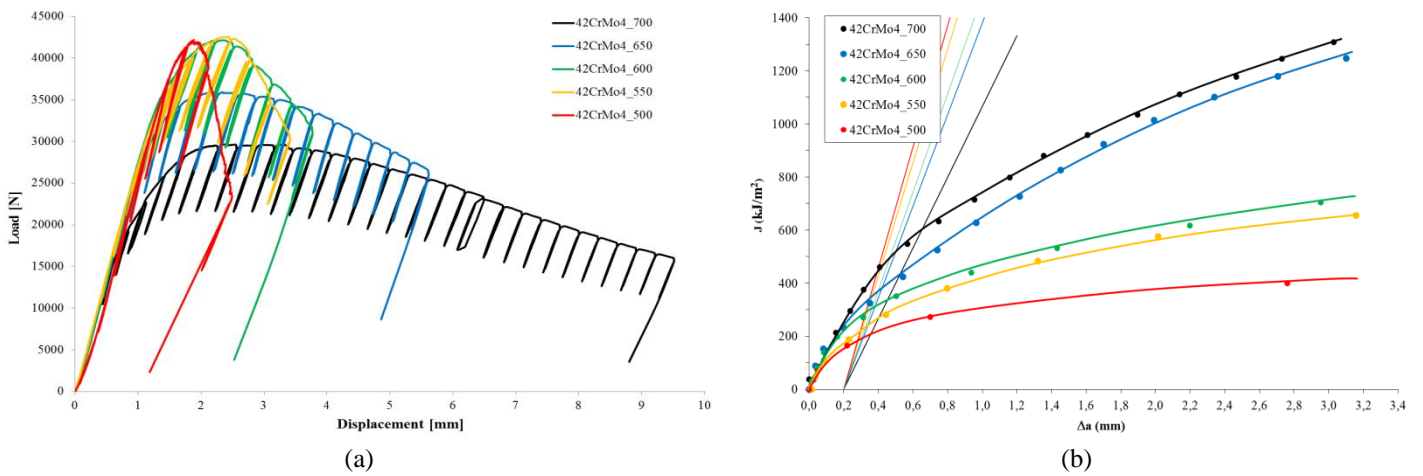
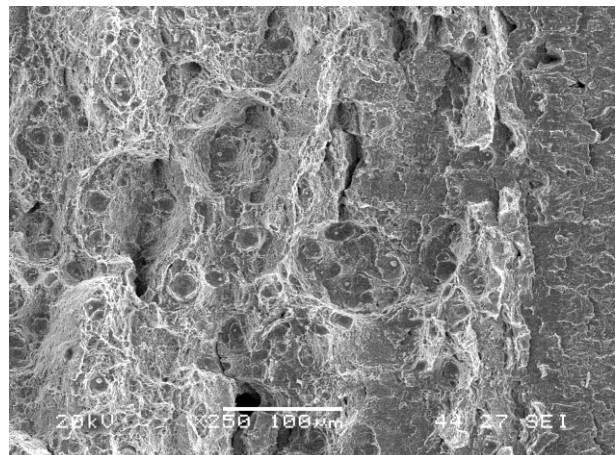
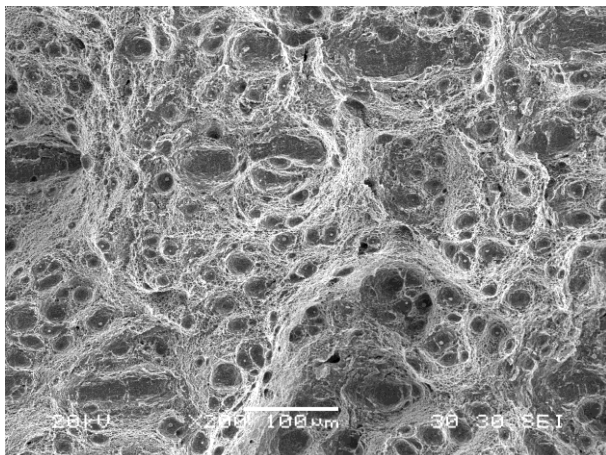


Figure 4. (a) Load-displacement and (b) J-resistance curves, corresponding to all the 42CrMo4 steel grades obtained with uncharged specimens.

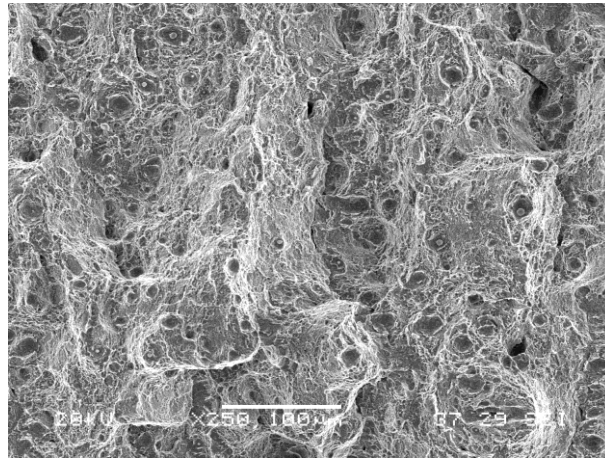
Steel Grade	σ_{ys} [MPa]	σ_{uts} [MPa]	V_{test} [mm/min]	P_{max} [N]	$J_{0.2/BL}$ [kJ/m ²]	$J=C_1\Delta a^{C_2}$	
						C_1	C_2
42CrMo4_700	622	710	1	29636	580	739	0.54
42CrMo4_650	820	905	1	35924	396	670	0.62
42CrMo4_600	880	985	1	42134	292	456	0.43
42CrMo4_550	1023	1113	0.1	42650	225	421	0.50
42CrMo4_500	1086	1198	0.1	41892	189	270	0.28

Table 5. Fracture toughness results of the different 42CrMo4 grades. Uncharged specimens.



(a) 42CrMo4_700 (Uncharged) 200x.

(c) 42CrMo4_600 (Uncharged) 250x.



(e) 42CrMo4_500 (Uncharged) 250x.

Figure 5. Fracture surface of uncharged CT specimens. (a) 42CrMo4_700, (b) 42CrMo4_600 (c) 42CrMo4_500.

3.2.2. Hydrogen pre-charged specimens

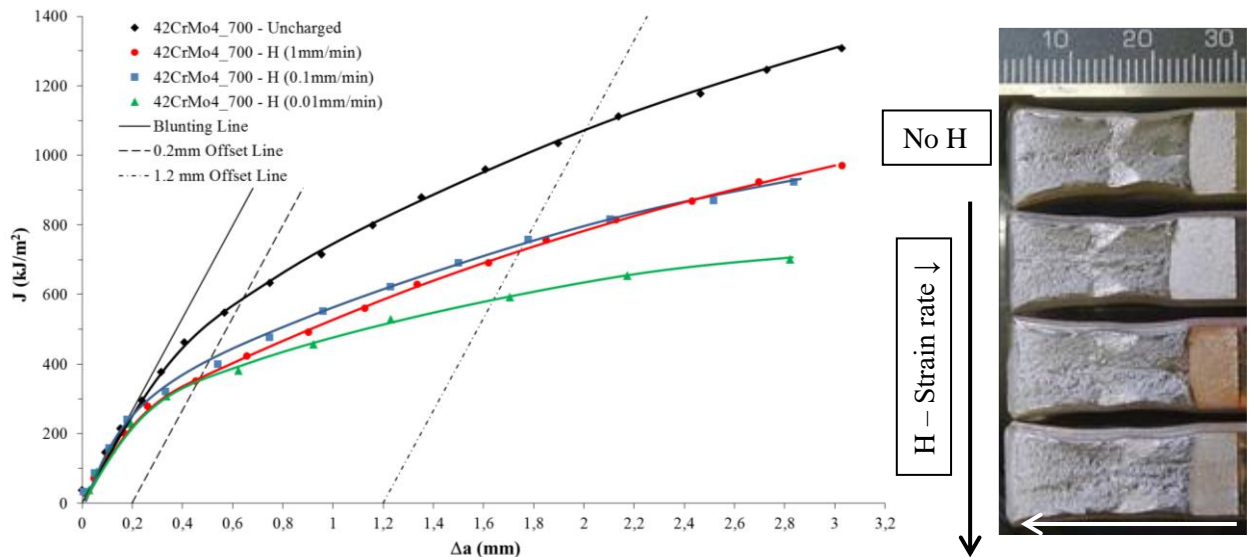
The results of all the fracture toughness tests performed on the different 42CrMo4 steel grades with uncharged and with hydrogen pre-charged specimens at the different applied displacement rates are collected in Table 6. Critical J value correspond to the value for the onset of crack growth, $J_{0.2/BL}$, in the case of grades quenched and tempered at 700, 650 and 600°C, and to unstable failure, J_Q , for grades quenched and tempered at 550 and 500°C. In this last case, J_Q value was derived from K_Q ($J_Q = K_Q^2(1-\nu^2)/E$). Additionally, the test duration, the evolution of hydrogen content along the test, the embrittlement index (EI) and the operative fracture micromechanisms (in order of importance) are also recorded. It is worth noting that C_H values in Table 6 may be taken with caution as they were derived from the desorption curves (Figure 2) obtained with samples with the same thickness (10 mm) but different geometry. Hydrogen desorption in CT specimens should be slower and therefore hydrogen content should be something higher.

Steel Grade	V_{test} [mm/min]	Test duration	C_H [ppm]	$J_{0.2/BL}$ [kJ/m ²]	EI ($J_{0.2/BL}$) [%]	*Fracture Micromechanisms
700	1	40min	-	580	-	MVC
	1	30min	1.2	350	40	MVC+PRHIC
	0.1	1.6h	1.2→1.1	380	34	MVC+PRHIC
	0.01	8.3h	1.2→0.8	345	41	MVC+PRHIC
650	1	28min	-	396	-	MVC
	1	22min	1.2	303	23	MVC+PRHIC
	0.1	80min	1.2	273	31	MVC+PRHIC
	0.01	6.7h	1.2→1	249	37	PRHIC
600	1	25min	-	292	-	MVC
	1	14min	1.4	205	30	MVC+PRHIC
	0.1	30min	1.4	175	40	MVC+PRHIC+IG
	0.01	2.6h	1.4→1.3	53	82	PRHIC+IG
Steel Grade	V_{test} [mm/min]	Test duration	C_H [ppm]	J_Q [kJ/m ²]	EI (J_Q) [%]	*Fracture Micromechanisms
550	0.1	18min	-	89	-	MVC
	0.1	25min	1.7	50	44	MVC+PRHIC+IG
	0.01	1h	1.7	19	79	PRHIC+IG+MVC
	0.001	1.7h	1.7	8	91	IG+PRHIC
500	0.1	40min	-	112	-	MVC
	0.1	12min	1.85	32	71	MVC+IG+PRHIC
	0.01	47min	1.85	8	93	IG+PRHIC
	0.001	1.8h	1.85	1	99	IG+PRHIC

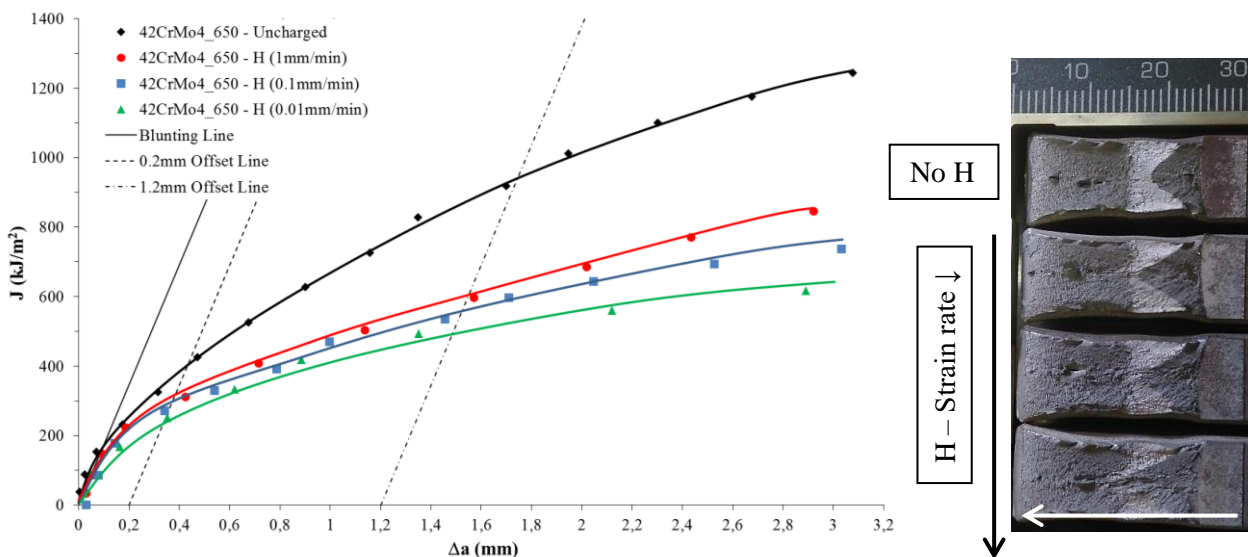
Table 6. Results of fracture toughness tests performed on the 42CrMo4 steel grades, uncharged and hydrogen pre-charged, loaded at different displacement rates ($J_Q = K_Q^2(1-\nu^2)/E$).

*MVC: microvoid coalescence; PRHIC: plasticity-related hydrogen induced cracking; IG: intergranular (in order of importance).

The J-resistance curves or J- Δa curves of the 42CrMo4 grade quenched and tempered at the highest temperature (700°C), corresponding to the steel with the lowest yield strength, obtained with uncharged and with H pre-charged specimens, at 1, 0.1 and 0.01 mm/min, are shown in Figure 6(a), along with their macroscopic fracture surfaces. The effect of hydrogen is noticeable, giving rise to a clear decrease of the whole curve and particularly the critical $J_{0.2/BL}$ parameter. Maximum embrittlement occurred under the lowest displacement rate, 0.01 mm/min. A decrease in fracture toughness when decreasing the displacement rate was also noted in the grades quenched and respectively tempered at 650 and 600°C (see Figure 6(b,c)).



(a)



(b)

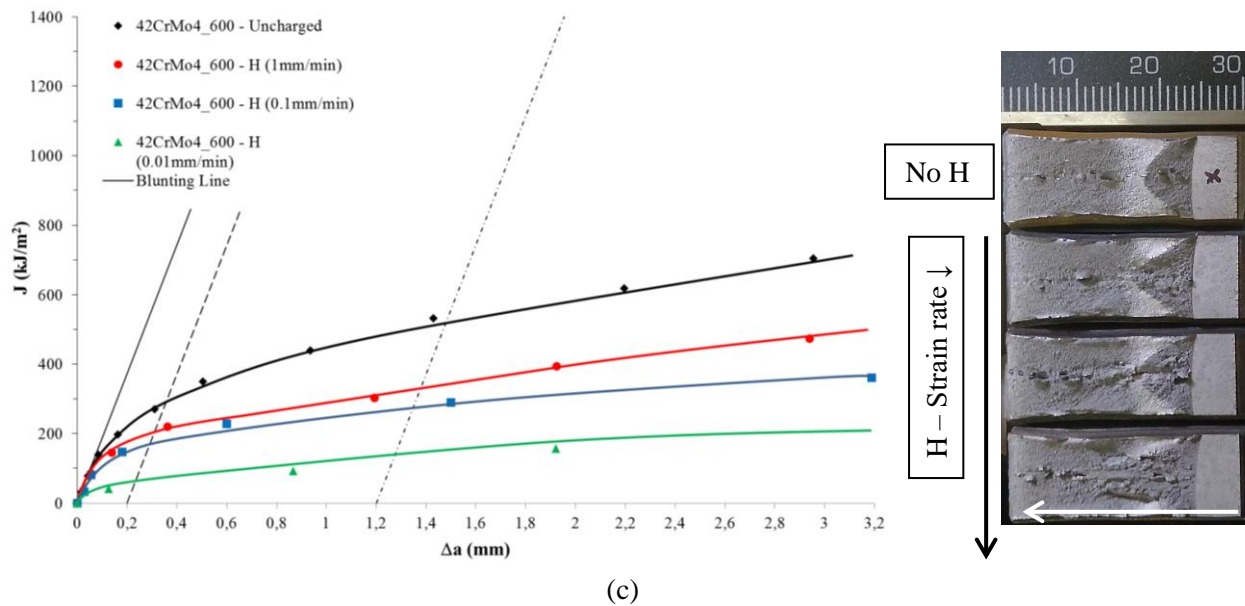
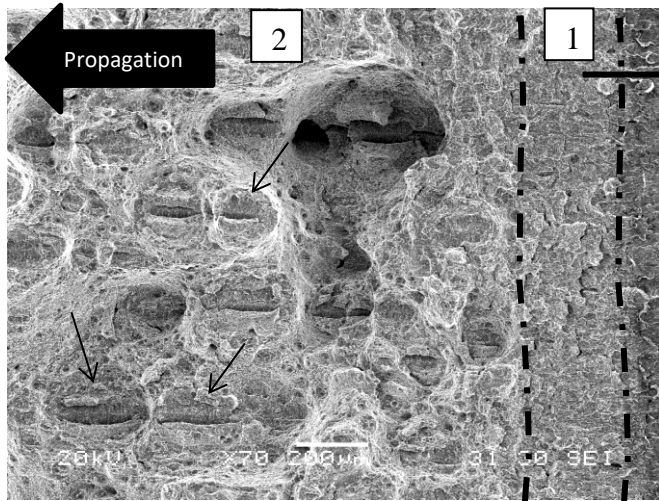


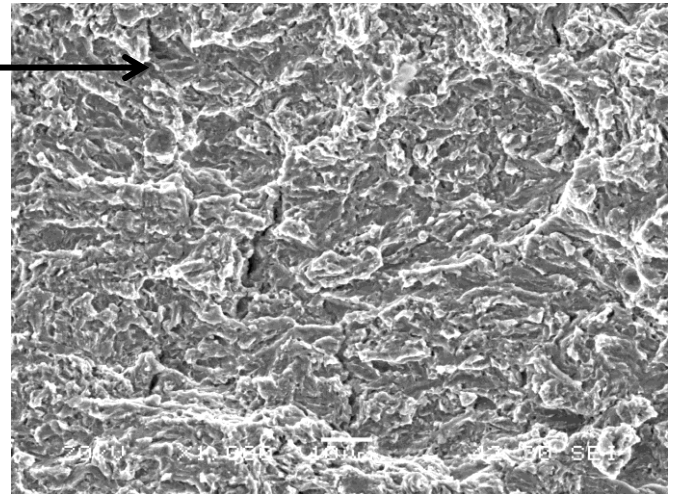
Figure 6. J - Δa curves and macroscopic fracture surfaces of uncharged and H pre-charged specimens tested at different displacement rates. (a) 42CrMo4_700, (b) 42CrMo4_650 and (c) 42CrMo4_600.

The fracture surface of the H pre-charged 42CrMo4_700 (under the lowest displacement rate) observed at SEM can be seen in Figure 7(a). Two different regions can be distinguished: region 1, with an extension of around 250 μm , corresponds to the initiation of the crack growth from the fatigue pre-crack, while region 2 corresponds to the propagation of the growing crack. Region 1, which can be seen in more detail in Figure 7(b), exhibits the appearance of a transgranular fracture surface or quasi-cleavage, usually referred to as plasticity-related hydrogen induced cracking (PRHIC) in martensitic steels [27]. The PRHIC mechanism was first described by Takeda and McMahon [36] in reference to the fracture mechanism observed in low alloy quenched and tempered steels in hydrogen gas. It is sometimes called tearing topography surface or TTS, which is described as a fracture surface characterised by ductile micro-plastic tearing on a very fine scale, along martensite lath, block and packet interphases [27, 37]. The size of the characteristic features observed in Figure 7(b) is comparable to the microstructure units (martensite blocks and packets); hence, hydrogen accumulation promotes plastic deformation and final decohesion of these interphases (HEDE, hydrogen-enhanced decohesion) [38]. On the other hand, a different micromechanism is observed in region 2 (Fig. 7(a)), where a fully ductile micromechanism, microvoids coalescence (MVC), is the prominent failure mechanism.

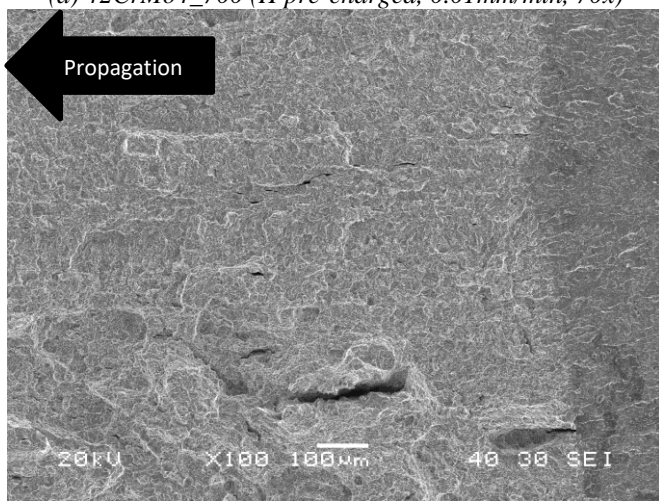
The embrittlement indexes and predominantly fracture micromechanisms corresponding to the steel grade quenched and tempered at 650°C for the different displacement rates, also shown in Table 6, are not so different from those observed in the 700°C tempered grade. As can be seen in Table 6, the fracture micromechanisms evolved from a fully ductile mechanism (MVC), in the absence of hydrogen, to 100% PRHIC, when tested under internal hydrogen at the lowest displacement rate (see Figure 7(c, d)). Mixtures of MVC and PRHIC micromechanisms were observed in hydrogen pre-charged specimens tested at intermediate displacement rates (Table 6). The hydrogen pre-charged steel grade quenched and tempered at 600°C tested at 0.1 mm/min already shows traces of IG fracture that finally, when tested at an even lower displacement rate, gives rise to a clear mixture of PRHIC and IG, as can be seen in Figure 7(e, f).



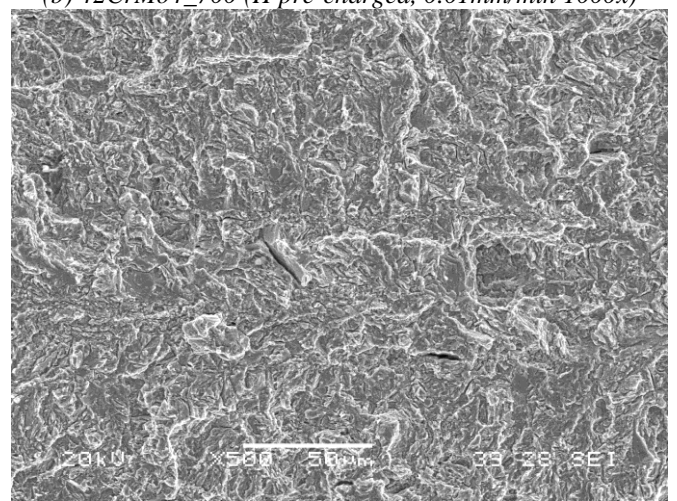
(a) 42CrMo4_700 (H pre-charged, 0.01mm/min, 70x)



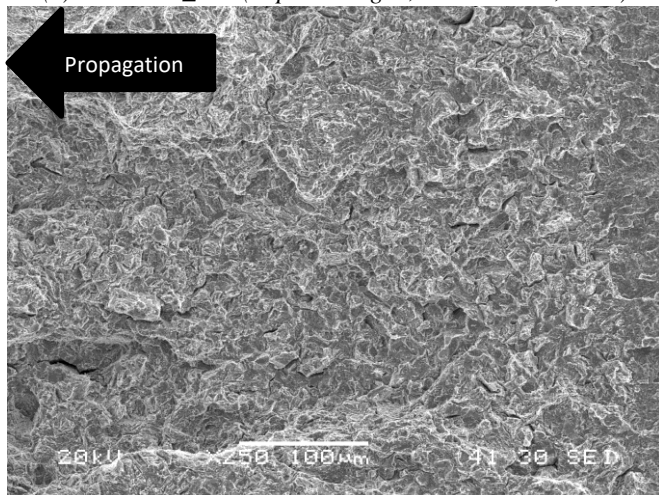
(b) 42CrMo4_700 (H pre-charged, 0.01mm/min 1000x)



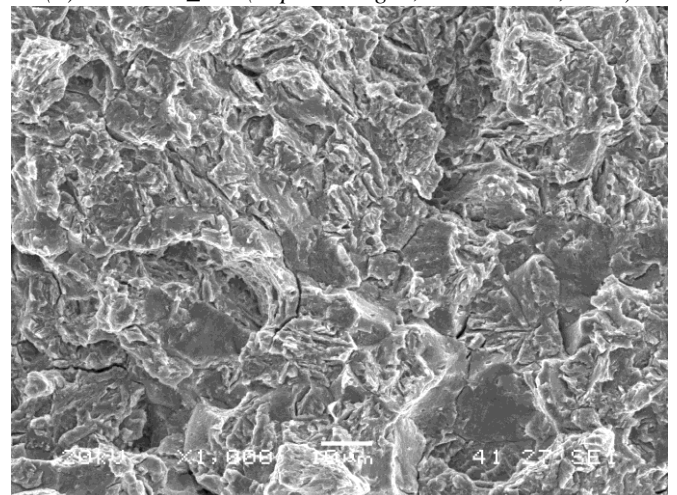
(c) 42CrMo4_650 (H pre-charged, 0.01mm/min, 100x)



(d) 42CrMo4_650 (H pre-charged, 0.01mm/min, 500x)



(e) 42CrMo4_600 (H pre-charged, 0.01mm/min, 250x)



(f) 42CrMo4_600 (H pre-charged, 0.01mm/min, 1000x)

Figure 7. Fracture micromechanisms of 42CrMo4 grades quenched and tempered at 700, 650 and 600°C tested with hydrogen at the lowest displacement rate.

Finally, the extreme brittleness of the H-charged 42CrMo4 steel grades quenched and tempered at the lowest temperatures (550 and 500°C) precluded obtaining J- Δa curves, so K_Q at instability (maximum load, P_Q) was used as a characteristic fracture toughness parameter. The load-displacement curves of the steel grade quenched and tempered at the lowest temperature, 500°C, along with their macroscopic fracture surfaces are presented in Figure 8(a). In the test carried out at 0.001mm/min, the deleterious effects of hydrogen are noteworthy: the load, P_Q , drops over 80% and the

embrittlement index relative to J_0 is practically equal to 100% (see Table 6). With regard to the fracture surfaces, as the displacement rate decreases, a clear evolution can be appreciated in the fracture micromechanisms. In this case, starting from MVC for the uncharged specimen, passing through a mixture of MVC, PRHIC and IG for the hydrogen pre-charged specimen tested at 0.1mm/min to finish in a micromechanism mainly composed of IG fracture, with faint remnants of PRHIC features, for the lowest displacement rate, as can be observed in Figure 9(c,d). Quite similar results were also obtained with the steel grade quenched and tempered at 550°C (Figure 8b): in the case of the test performed at the lowest displacement rate, the predominant micromechanism is IG, with isolated regions of PRHIC, Figure 9 (a,b).

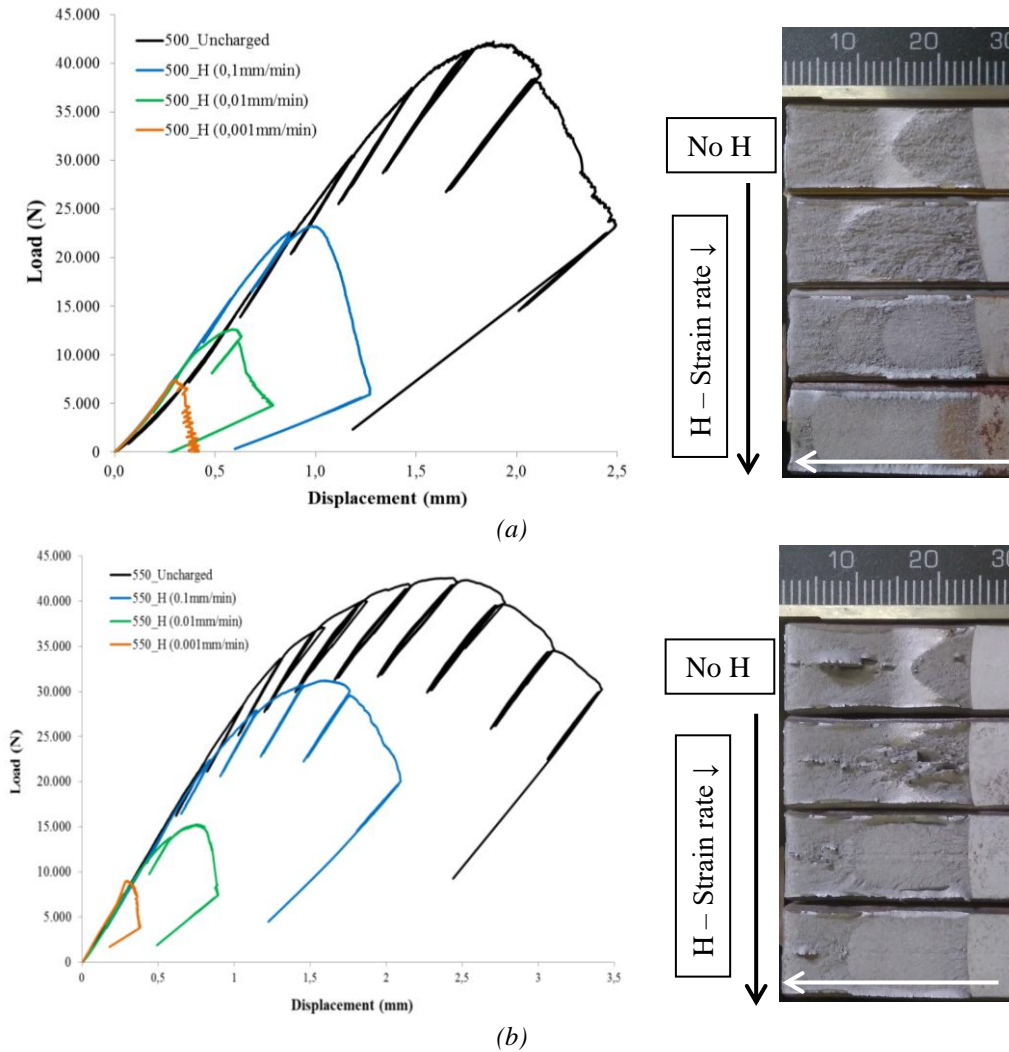


Figure 8. Load versus load line displacement (LLD) curves and macroscopic fracture surfaces corresponding to the 42CrMo4 steel quenched and tempered at (a) 500°C and (b) 550°C. Uncharged specimen and H pre-charged specimens tested at 0.1, 0.01 and 0.001mm/min.

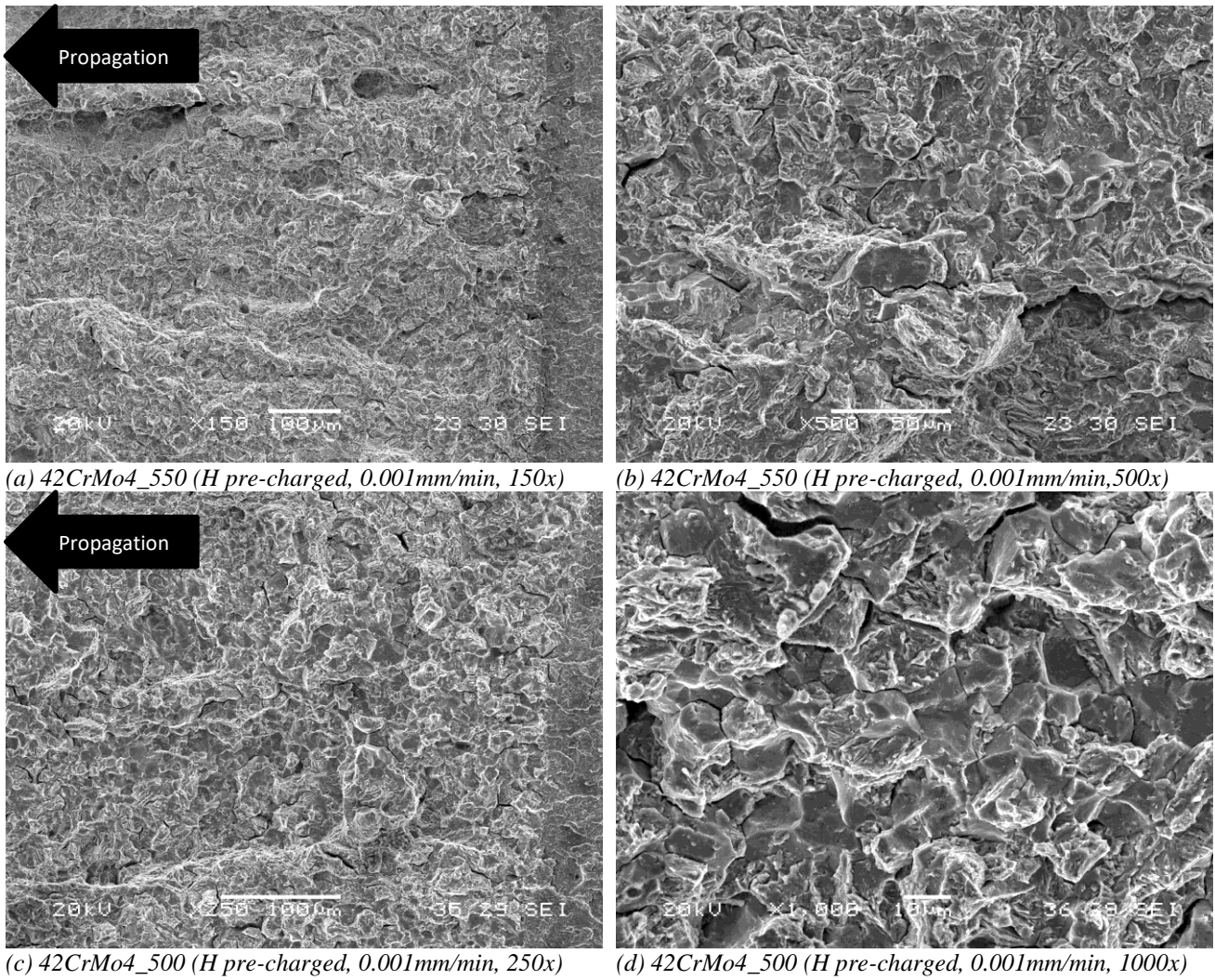
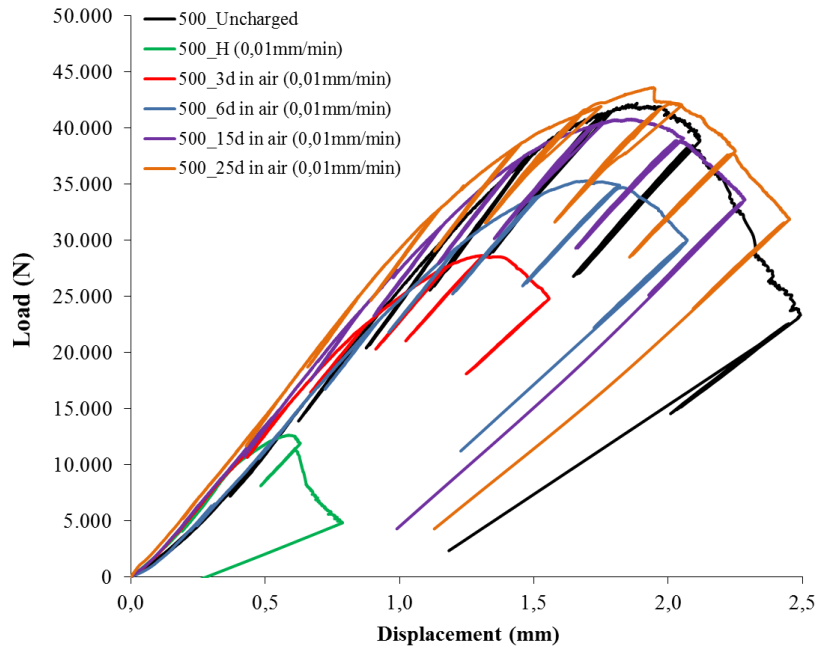


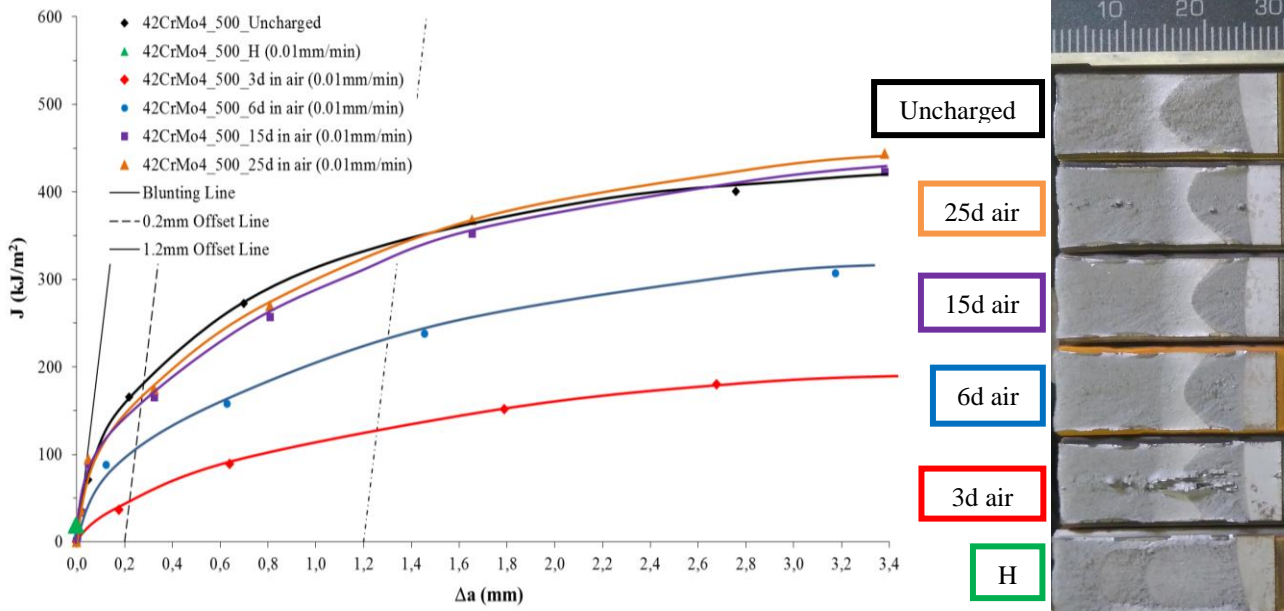
Figure 9. Fracture micromechanisms of 42CrMo4 grades quenched and tempered at 550 and 500°C tested with hydrogen at the lowest displacement rate.

3.2.3. Room temperature de-embrittlement of 42CrMo4_500

Figure 10(a) shows the load-displacement curves corresponding to fracture toughness tests of hydrogen pre-charged 42CrMo4_500 steel grade after degassing the CT specimens at room temperature during 3, 6, 15 and 25 days. The same curves obtained with the uncharged specimen and just after hydrogen pre-charging are also included. All the tests were performed at the same displacement rate of 0.01mm/min. Additionally, the J-resistance curves, J parameter versus crack growth curves, J- Δa , along with macroscopic fracture surfaces are shown in Figure 10(b). Only the test performed just after hydrogen pre-charging was unable to give a J- Δa curve and, in this case, the J_Q value at failure instability (obtained from the K_Q value) was represented in the same plot as a green triangle. Firstly, as mentioned previously, it can be observed the great difference between the behaviour of uncharged specimens (black curve in Fig. 10(a)) and H pre-charged specimens tested immediately after hydrogen pre-charge (green curve in the same figure). An intermediate behaviour was obtained after degassing the specimen during 3 and 6 days in air at RT, and finally, specimens degassed respectively for 15 and 25 days showed a behaviour almost identical to the one manifested by the uncharged specimens. All the fracture toughness values, embrittlement indexes, degas times, testing duration times, and operative fracture micromechanisms in order of importance are gathered in Table 7.



(a)



(b)

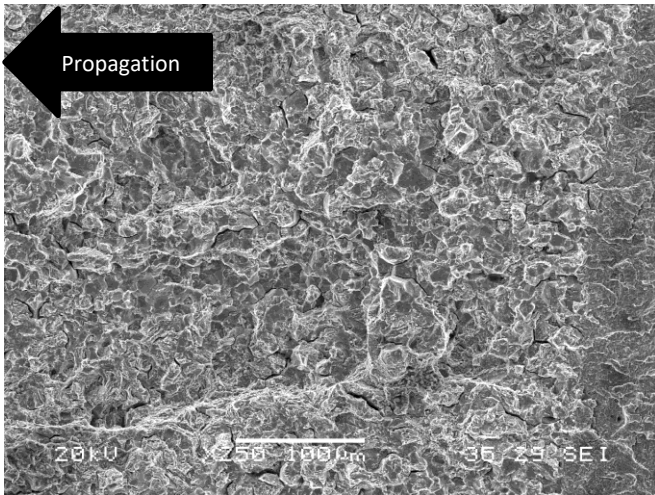
Figure 10. (a) Load – load line displacement (LLD) curves and (b) J - Δa curves (and macroscopic fracture surfaces) corresponding to the 42CrMo4 steel quenched and tempered at 500°C, tested at 0.01mm/min. Uncharged, tested just after charging and after 3, 6, 15 and 25 days degassing in air.

Steel Grade	V_{test} [mm/min]	Time in air [days]	Test duration	C_H [ppm]	$J_{0.2/BL}$ [kJ/m ²]	Fracture Micromechanisms	
						EI ($J_{0.2/BL}$) [%]	Initiation Propagation
500	0.1	-	40min	-	189	---	MVC
	0.01	-	47min	1.85	8 (J_Q) ⁽¹⁾	97	IG+PRHC
	0.01	3	2.2h	1.71	43	78	IG+PRHC
	0.01	6	3.2h	1.62	115	40	IG+PRHC MVC
	0.01	15	3.5h	1.55	168	11	PRHC MVC
	0.01	25	3.8h	1.50	178	6	MVC

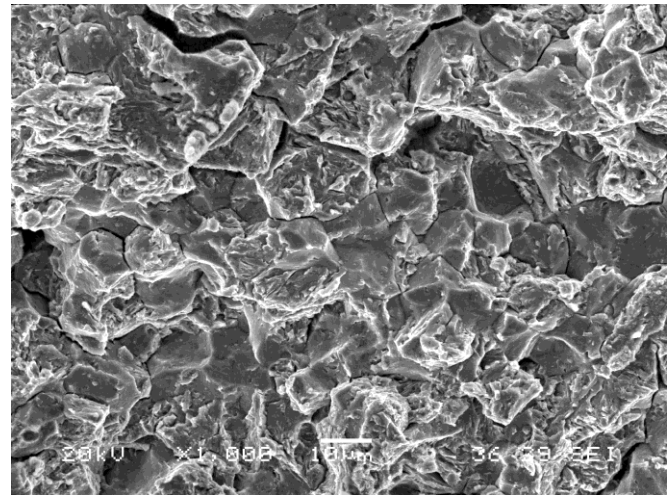
Table 7. Fracture toughness recovery of 42CrMo4_500 steel grade after degassing for different times.

⁽¹⁾ derived from K_Q ($J_Q = K_Q^2(1-\nu^2)/E$).

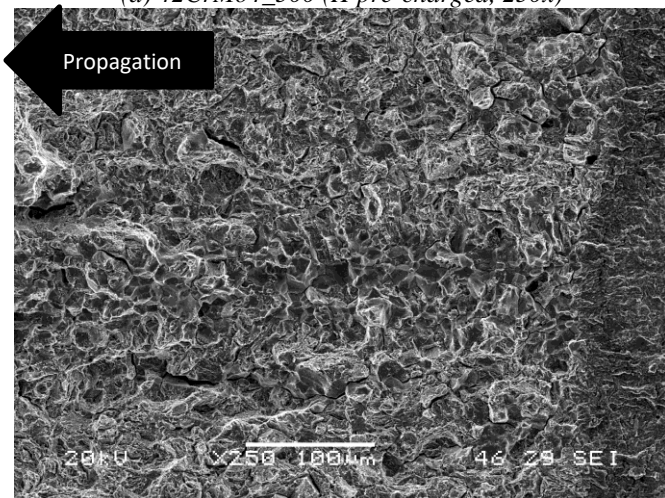
The fracture micromechanisms observed on these specimens are presented in Figure 11. The specimen tested after 3 days at RT in air, Fig. 11(c,d) still shows the typical mixed IG+PRHIC fracture micromechanisms, already observed in the hydrogen pre-charged and no-degassed specimen (Fig. 11(a,b)). After 6 days in air, Fig. 11(e), the fracture micromechanism starts changing: an initiation area of around 2.5 mm, (1) in the figure, characterized by a mixture of PRHIC and IG is observed, followed by MVC, (2) in the same figure. Enlarged views of these two regions are shown in Figures 11(f,g) respectively. After 15 days of degassing, the main fracture micromechanism is MVC, except from a very narrow band at the beginning of the fracture surface where PRHIC was detected (Figures 11(h,i)). Finally, the specimen left at RT in air 25 days before the test only exhibits MVC (Figures 11(j,k)), exactly as already observed in the uncharged specimen (Figure 5 (e)).



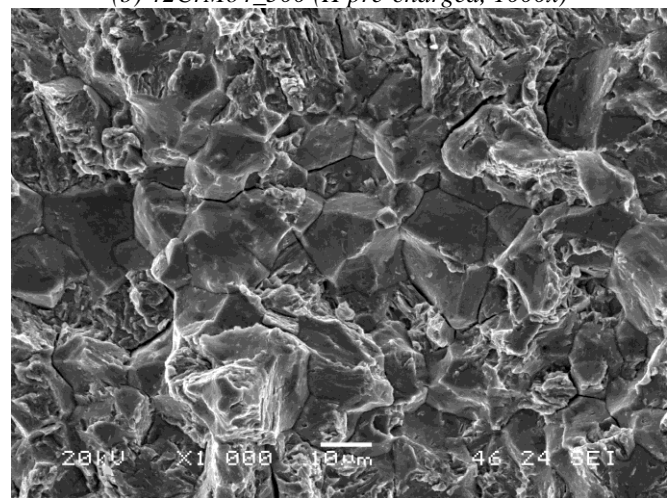
(a) 42CrMo4_500 (H pre-charged, 250x)



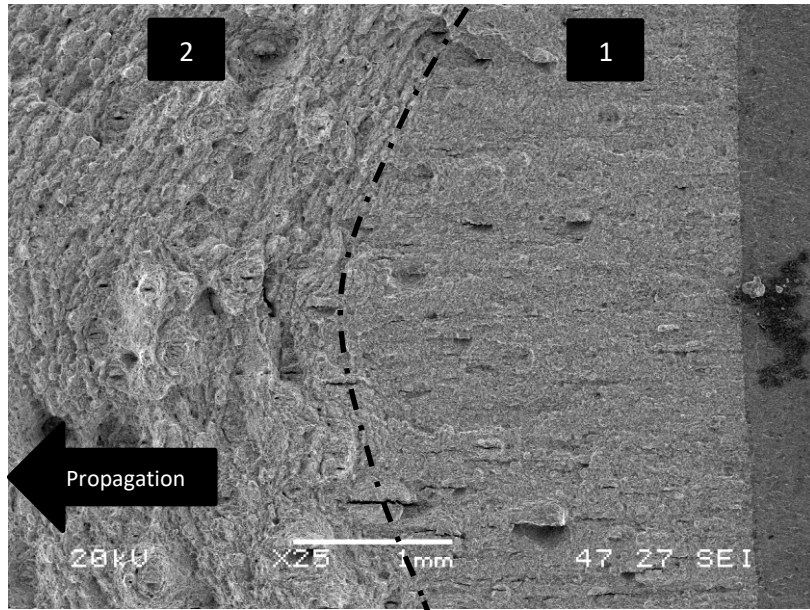
(b) 42CrMo4_500 (H pre-charged, 1000x)



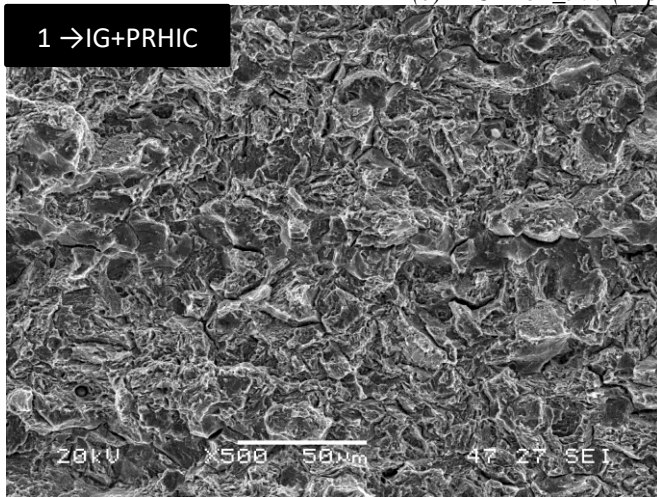
(c) 42CrMo4_500 (H pre-charged, 3d in air, 250x)



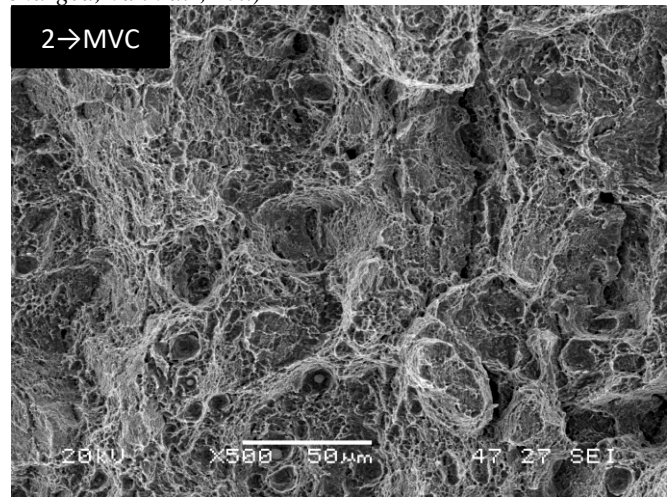
(d) 42CrMo4_500 (H pre-charged, 3d in air, 1000x)



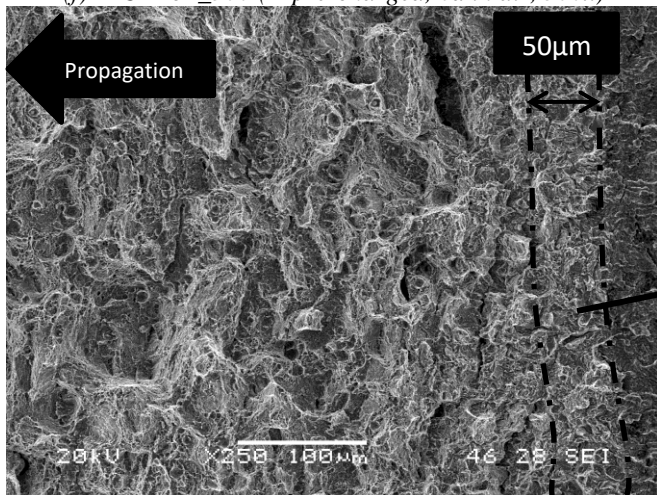
(e) 42CrMo4_500 (H pre-charged, 6d in air, 25x)



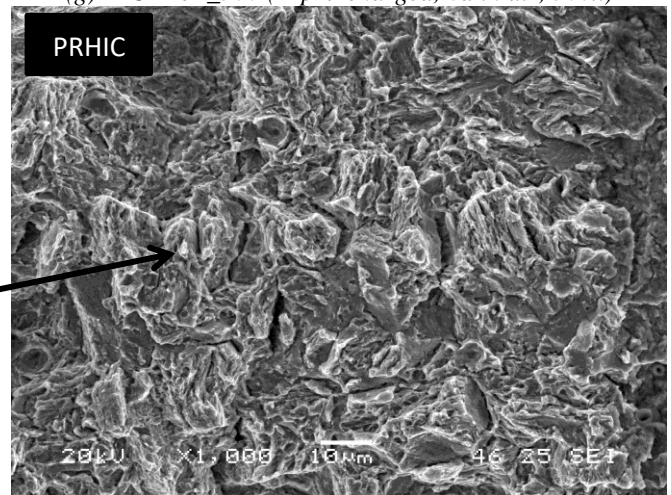
(f) 42CrMo4_500 (H pre-charged, 6d in air, 500x)



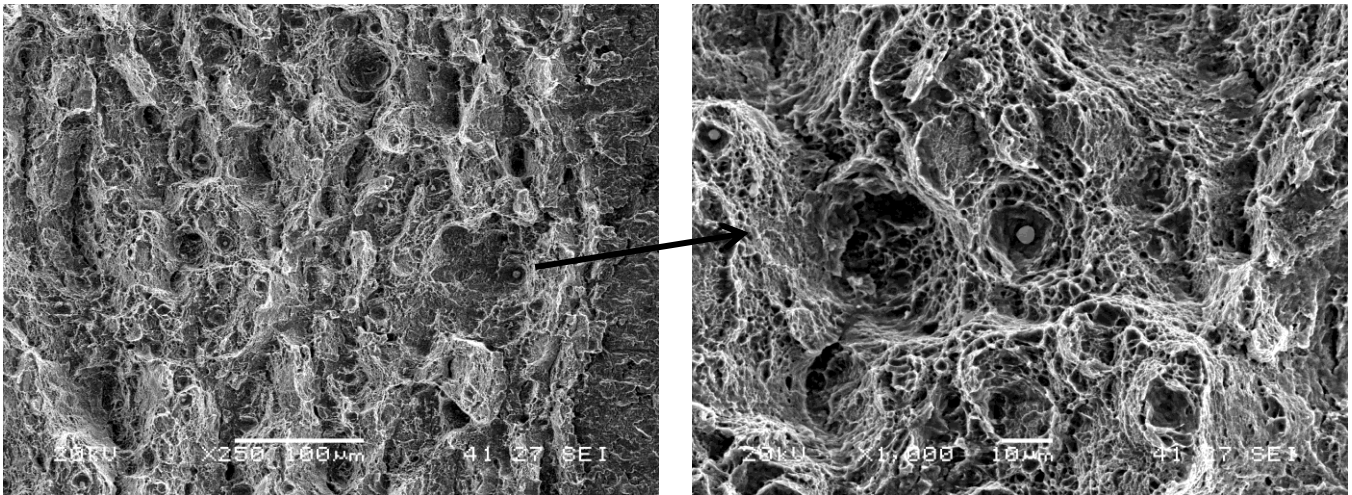
(g) 42CrMo4_500 (H pre-charged, 6d in air, 500x)



(h) 42CrMo4_500 (H pre-charged, 15d in air, 250x)



(i) 42CrMo4_500 (H pre-charged, 15d in air, 1000x)



(j) 42CrMo4_500 (H pre-charged, 25d in air, 250x)

(k) 42CrMo4_500 (H pre-charged, 25d in air, 250x)

Figure 11. Fracture micromechanisms of H pre-charged 42CrMo4_500 steel grade after degassing for different times and tested at 0.01mm/min.

4. Discussion

The tempered martensite microstructure of the quenched and tempered 42CrMo4 grades is especially dependent on the tempering temperature. As tempering temperature increases from 500 to 700°C (two hours), carbide precipitate, internal residual stresses relax and dislocation density reduces. According to results exposed in Table 4, the initial hydrogen content, measured in samples pre-charged under high temperature and high hydrogen pressure, increased with decreasing steel tempering temperature, due to the fact that hydrogen microstructural trapping is greater in distorted, high energy martensitic microstructures (with high dislocation densities). Moreover, the final hydrogen content (residual hydrogen), hydrogen strongly trapped in the steel microstructure, is even more dependent on the steel microstructure, decreasing with increasing tempering temperature, mainly due to stress relaxation and the reduction in dislocation density and interphases (martensite laths, blocks and packets).

Apart from the effect that tempering temperature has on the tensile and fracture toughness properties of the steel, dislocation density, hydrogen trapping and apparent hydrogen diffusion coefficients were also significantly modified. As tempering temperature increases, it was observed that dislocation density decreases (Table 3) and also hydrogen trapping does (Table 4), but the apparent hydrogen diffusion increases (Table 4). Figure 12(a) shows in a graphic way the evolution of the dislocation density and the apparent diffusion coefficient with the steel tempering temperature, while Figure 12(b) shows a linear correlation between the hydrogen retained in the steel (residual hydrogen present after very long times at room temperature, hydrogen strongly trapped in the steel microstructure) and the dislocation density. Quite high R^2 determination coefficients were obtained in all these correlations.

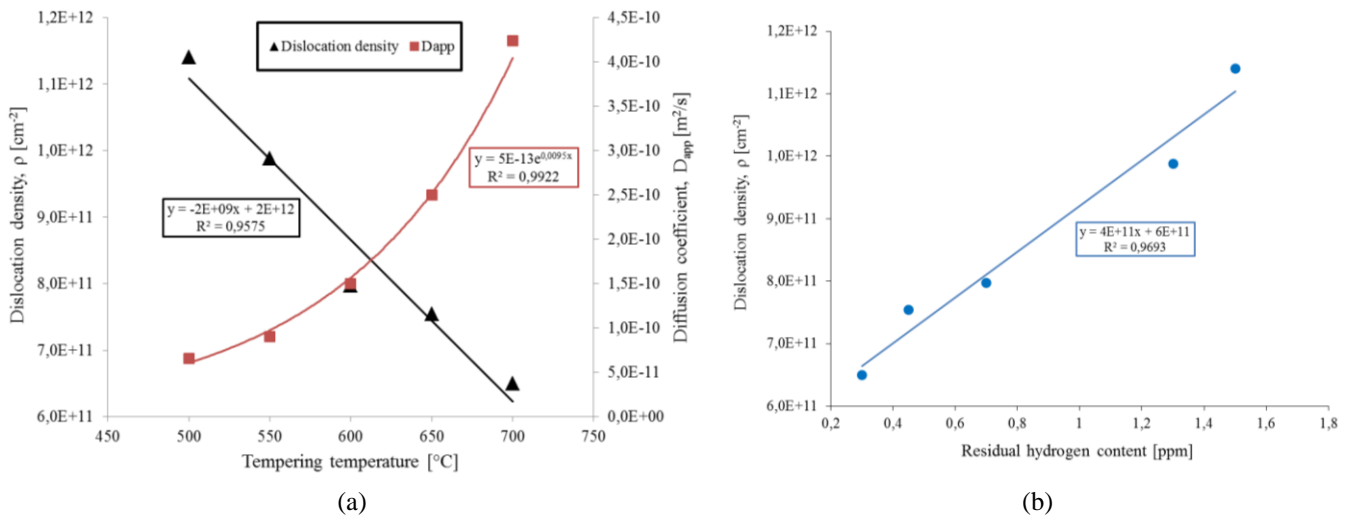


Figure 12. (a) Evolution of dislocation density and diffusion coefficient with the tempering temperature. (b) Dislocation density versus residual hydrogen (after charging in high pressure hydrogen gas).

On the other hand, the fracture toughness reduction due to the presence of internal hydrogen in the microstructure of all these steels is noticeable, giving rise to a clear decrease of the whole J-resistance curve and particularly on the critical J parameter for the onset of crack growth, $J_{0.2/BL}$ or J_Q . Maximum embrittlement occurred in the grades tempered at the lowest temperatures (higher hardness and yield strength) and when tested under the lowest displacement rates.

In order to justify the fracture toughness results obtained in this study, it should be first at all recalled the stress and strain distribution existing ahead of a cracked, stress loaded elasto-plastic material (CT specimen). The stress reaches a peak that, according with the continuum plasticity theory, is located at a distance x from the crack tip, $x=J/\sigma_{ys}$ [39, 40]. Moreover, local strain exhibits a singularity at the crack tip, reaching very high values ($\epsilon_{eq}>10\%$) at approximately half this distance ($J/2\sigma_{ys}$), where the dislocation density multiplies, giving rise to high local hydrogen accumulation. The maximum levels of the normal opening stress, σ_{yy} , and the hydrostatic stress, σ_H , are respectively about $3.5 \sigma_{ys}$ and $2.5 \sigma_{ys}$. Moreover, hydrogen located in the surroundings of the crack will diffuse up to the process zone located just ahead of the crack tip (driven by the high hydrostatic stress existing in the crack front, where it is also trapped by dislocations entanglements produced in the plastic strained zone), where hydrogen atoms will accumulate, giving rise to the embrittlement phenomenon (hydrogen enhanced decohesion, HEDE). According to Oriani theory [41], hydrogen atoms are attracted by the hydrostatic stress existing ahead of the crack until an equilibrium hydrogen concentration, c_H , given by Equation (7) is attained:

$$c_H = c_0 \cdot e^{(\sigma_H V_H / RT)} \quad (7)$$

where, c_0 is the hydrogen value at zero stress and V_H is the partial molar volume of hydrogen, which can be approximated by $2 \cdot 10^{-6} \text{ m}^3/\text{mol H}$ in a ferritic microstructure.

Hence, the influence of the steel yield strength in the fracture toughness embrittlement is explained by its effect on the level of the hydrostatic stress produced ahead of the crack tip, σ_H , and consequently, on the hydrogen content, c_H , accumulated in the process zone, while the influence of the test displacement rate on the fracture toughness properties will depend on the time that hydrogen has to diffuse and accumulate until reaching a critical concentration in the aforementioned process zone (see Figure 13).

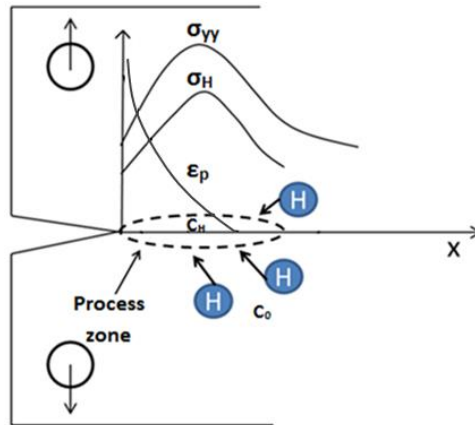


Figure 13. Hydrogen diffusion towards the process zone ahead of an opened crack tip. σ_{yy} , σ_H and ϵ_p are respectively the opening stress, hydrostatic stress and plastic strain.

Taking into account the values of $J_{0.2/BL}$ measured in the 42CrMo4_700 grade under the lowest displacement rate (345 kJ/m^2 , Table 6) and the yield strength of this steel (622 MPa), the extension of the high strained process region where hydrogen accumulates ($x=J/2\sigma_{ys}$) would be $280 \mu\text{m}$, which is nearly the same value measured for the extension of region 1 shown in Fig. 7(a), about $250 \mu\text{m}$, where PRHC micromechanism was seen to be prevalent. Hydrogen accumulation in this region promotes decohesion of internal interphases, such as martensite laths, blocks and packets (HEDE, hydrogen-enhanced decohesion). On the other hand, a different micromechanism is observed in region 2 (Fig.

7(a)), away from the region submitted to high triaxiality, where microvoids coalescence, MVC, is now the prominent failure micromechanism. As the applied J increases, the plastic zone extends, diffusible hydrogen redistributes into a larger volume and, hence, the total local hydrogen content in the process zone decreases and PRHIC is no longer available (MVC appears instead). Similar facts were also observed in the steels grades quenched and tempered at 650°C and at 600°C, although due to their higher yield strengths (820 and 880 MPa respectively), hydrogen accumulation in the crack front region increases and embrittlement phenomena also does. Higher accumulation of hydrogen in the process zone in the steel grade quenched and tempered at 600°C (with higher yield strength) tested at low displacement rates (0.1 and 0.01 mm/min, Table 6) gave also rise to failed regions by intergranular fracture (IG), that is decohesion along their prior austenite grain boundaries.

Finally, the extreme brittleness of the H pre-charged 42CrMo4 steel grades quenched and tempered at the lowest temperatures (550 and 500°C) is justified by their much higher yield strengths (1023 and 1086 MPa respectively) and, consequently, much higher hydrogen accumulation, C_H , in the process zone takes place, a significant fraction of their prior austenite grain boundaries is embrittled and final decohesion takes place when an enough low displacement rate is applied.

Figure 14 represents the critical stress intensity factor ($J_{0.2/BL}$ or J_Q) for the onset of crack growth measured with hydrogen pre-charged specimens under a low displacement rate of 0.01 mm/min versus the tempering temperature (yield strength) for the quenched and tempered 42CrMo4 steel grades. The predominant fracture micromechanisms are also shown in the figure. The sudden drop in fracture toughness under internal hydrogen and low displacement rate when intergranular failure micromechanism appears (steel grade quenched and tempered at 600°C, $\sigma_{ys} = 880$ MPa) are worth noting. As can be seen in Fig. 1(c), the quenched and tempered microstructure of this steel still shows elongated carbides precipitated along prior austenite grain boundaries and block and packet martensite boundaries, resembling low tempering microstructures (steel grades tempered at 550°C and 500°C). These distorted internal interphases are able to trap and retain hydrogen (0.7 ppm H is strongly trapped, as can be seen in Table 4). Additionally, diffusible hydrogen (0.7 ppm) moves and accumulates in the process zone ahead of the crack tip of the CT specimen (within the plastic zone with a high dislocation density and at the region submitted to high hydrostatic stress), giving rise to a HEDE failure micromechanism (hydrogen-enhanced decohesion, PRHIC and intergranular fracture, IG). However, 42CrMo4 steel quenched and tempered at 650 and at 700°C already have sufficiently relaxed quenched and tempered microstructures with quite uniform dispersion of globular carbides (see Figure 1(a,b)), so hydrogen distributes in a more uniform manner in the crack front process region, giving rise to decohesion of packet and block martensite boundaries (PRHIC) only after significant previous plastic deformation (high fracture toughness for the onset of crack growth). Anyway, the extreme brittleness of the H-charged 42CrMo4 steel grades tempered at the lowest temperatures (500, 550°C and even at 600°C) excludes the use of these steel grades when toughness is a design requirement.

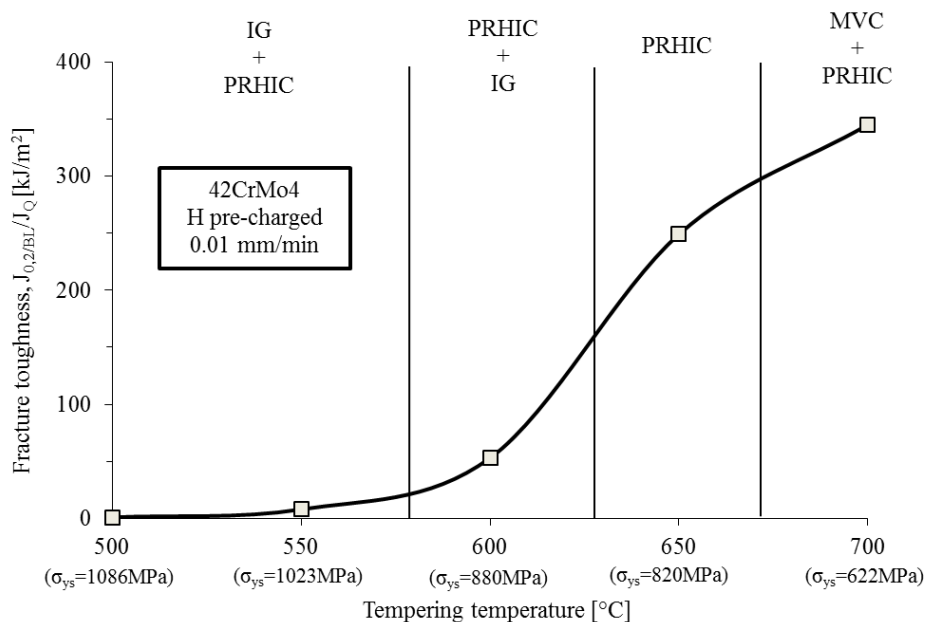


Figure 14. Fracture toughness for the onset of crack growth with internal hydrogen versus the tempering temperature (yield strength) in quenched and tempered 42CrMo4 steel and predominant operative failure micromechanisms.

Regarding finally the effect of room temperature degassing the CT specimens of the 42CrMo4 steel quenched and tempered at 500°C (the grade most susceptible to hydrogen-embrittlement) during several days, a very good correlation was obtained between the measured fracture toughness and the diffusible hydrogen, as it can be seen in Figure 15. Diffusible hydrogen was obtained using the desorption curve presented in Figure 2. As it was already mentioned, these diffusible hydrogen data are only a qualitative approximation, as they were obtained using samples with the same sample thickness but different geometry.

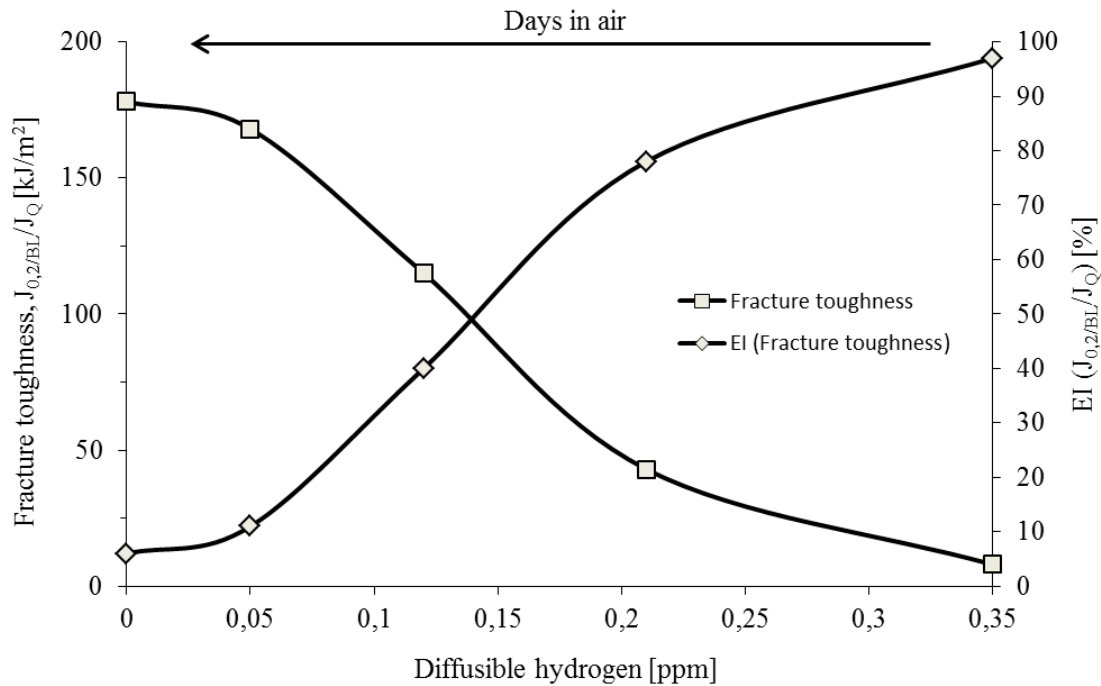


Figure 15. Critical fracture toughness, $J_{0.2/BL}$ or J_Q and EI, versus diffusible hydrogen. 42CrMo4_500 steel grade.

Anyway, these results lead us to the conclusion that only diffusible hydrogen, hydrogen which is able to move through the microstructure and overcome traps, is able to damage the steel microstructure and trigger hydrogen-related fracture micromechanisms (PRHC and IG) but, once only strongly trapped hydrogen remains in the specimen and diffusible hydrogen approaches to zero, the so-called residual hydrogen (1.5 ppm, after 25 days degassing treatment in this case, Table 7), its behaviour is the same as the one obtained with the hydrogen free specimen. The relationship between the operative fracture micromechanism and the diffusible hydrogen can also be observed on the fracture surface of the CT specimen de-gassed for 15 days at RT (Fig. 11(h)). Using the fracture toughness measured in this specimen (168 kJ/m², Table 7) and the yield strength of this steel (1086 MPa), the extension of the high strained process region ($x=J/2\sigma_{ys}$) is 77 μm , while the extension of the PRHC region measured in Fig. 11(h) is not much different, around 55 μm .

5. CONCLUSIONS

Using a 42CrMo4 steel quenched and tempered at different temperatures to obtain tempered martensite microstructures, it was demonstrated that as tempering temperature is increased, yield strength and hardness decrease but elongation and fracture toughness increase. Consequently, dislocation density and residual hydrogen measured in samples pre-charged under high pressure high temperature hydrogen gas (hydrogen strongly trapped in the steel microstructure) decrease, while the apparent diffusion coefficient increases. A linear correlation was obtained between the tempering temperature and the dislocation density and also between this last characteristic and the hydrogen retained at RT in the steel.

On the other hand, the fracture toughness reduction due to the presence of internally pre-charged hydrogen in the microstructure of all these steels is noticeable, giving rise to a clear decrease of the whole J-resistance curve and particularly on the critical J parameter for the onset of crack growth, $J_{0.2/BL}$ or J_Q . Maximum embrittlement occurred in

the grades tempered at the lowest temperatures (higher hardness and yield strength) and when tested under the lowest displacement rate. These fracture toughness results were justified because hydrogen accumulation in the process zone located in the front of the crack tip in the CT specimen depends on the local hydrostatic stress and this parameter is related to the steel yield strength: as the yield strength of the steel increases, the hydrostatic stress and the hydrogen content accumulated in the process zone also increase, giving rise to a whole change in the failure micromechanism, from a fully ductile one, microvoids coalescence (MCV), to decohesion along martensite lath, block and packet interphases (PRHIC) or even decohesion along prior austenite grain boundaries (IG), in the case of the grades with the highest yield strength or tempered at the lowest temperatures. Moreover, the use of lower displacement rates always gave rise to higher hydrogen embrittlement indexes, as the accumulation of hydrogen atoms in the most stressed area of the fracture specimen increases due to the availability of longer diffusion times.

Finally, room temperature degassing experiments with the CT specimens allowed us to obtain a very good correlation between the measured fracture toughness and the diffusible hydrogen, so that only diffusible hydrogen, hydrogen able to move along the steel microstructure at the test temperature, RT in this particular case, can trigger hydrogen-related interphase decohesion fracture micromechanisms, while the presence of residual hydrogen strongly trapped by the steel microstructure is, by the contrary, non-relevant for this purpose.

ACKNOWLEDGEMENTS

The authors would like to thank the Spanish Ministry of Economy and Competitiveness for the support received to carry out research project MAT2014-58738-C3 (SAFEHIDROSTEEL) and also to the Principado de Asturias government for the financing support given through the IDI/2018/000134 project.

REFERENCES

- [1] J. Yamabe, T. Awane, and S. Matsuoka, Investigation of hydrogen transport behavior of various low-alloy steels with high-pressure hydrogen gas, *Int. J. Hydrogen Energy* 40(34) (2015) 11075–11086.
- [2] J. H. Chuang, L. W. Tsay, and C. Chen, Crack growth behaviour of heat-treated 4140 steel in air and gaseous hydrogen, *Int. J. Fatigue* 20(7) (1998) 531–536.
- [3] Hilkes J., Gross V., *Welding Cr-Mo steels for power generation and petrochemical applications – past, present and future*, IIW conference, Singapore, 2009. pp. 12-22
- [4] Y. Takeda and C. J. McMahon Jr., Strain controlled vs. stress controlled hydrogen induced fracture in a quenched and tempered steel, *Metall. Mater. Trans. A* 12 (1981) 1255–1266.
- [5] L. Briottet, R. Batisse, G. de Dinechin, P. Langlois, and L. Thiers, Recommendations on X80 steel for the design of hydrogen gas transmission pipelines, *Int. J. Hydrogen Energy* 37(11) (2012) 9423–9430.
- [6] A. Zafra, L.B. Peral, J. Belzunce, C. Rodríguez, Effect of hydrogen on the tensile properties of 42CrMo4 steel quenched and tempered at different temperatures, *Int. J. of Hydrogen Energy* 43(2018) 9068-9082.
- [7] M. Tvrđý, S. Havel, L. Hyspecká and K. Mazanec, Hydrogen embrittlement of CrMo and CrMoV pressure vessel steels, *Int. J. of Pres. Ves. Piping* 9 (1981) 355-365.
- [8] D.R.G. Mitchell, C.J. Moss, R.R. Griffiths, Optimisation of post-weld heat treatment of a 1.25Cr-0.5Mo pressure vessel for high temperature hydrogen service, *Int. J. of Pres. Ves. Piping* 76 (1999) 259-266.
- [9] K. Shen, L. Xu, Y. Guo, J. Shi, M. Wang, Effect of microstructure on hydrogen diffusion and notch tensile strength of large steel forging, *Mater. Sci. Eng. A* 628, pp. 149-153. 2015.
- [10] Y. Zhao, M.Y. Seok, I.C. Choi, Y.H. Lee, S.J. Park, U. Ramamurty, J.Y. Suh, J.I. Jang, The role of hydrogen in hardening/softening steel: Influence of the charging process, *Scripta Mater.* 107 (2015) 46-49.
- [11] M. Wang, E. Akiyama and K. Tsuzaki, Effect of hydrogen and stress concentration on the notch tensile strength of AISI41, *Mater. Sci. Eng. A* 398 (2005) 37-46.
- [12] S. Takagi, S. Terasaki, K. Tsuzaki, T. Inoue and F. Minami, Application of local approach to hydrogen

embrittlement fracture evaluation of high strength steels, *Mater. Sci. Forum* 539-543 (2007) 2155-2161.

- [13] M. Wang, E. Akiyama and K. Tsuzaki, Crosshead speed dependence of the notch tensile strength of a high strength steel in presence of hydrogen, *Scripta Mater.* 53 (2005) 713-718.
- [14] M. Wang, E. Akiyama, and K. Tsuzaki, Effect of hydrogen on the fracture behavior of high strength steel during slow strain rate test, *Corros. Sci.* 49(11) (2007) 4081–4097.
- [15] Y. Momotani, A. Shibata, D. Terada, N. Tsuji, Effect of strain rate on hydrogen embrittlement in low-carbon martensitic steel, *Int. J. Hydrogen Energy* 42 (2017) 3371-3379.
- [16] Y. Murakami and S. Matsuoka, Effect of hydrogen on fatigue crack growth of metals, *Eng. Fract. Mech.* 77(11) (2010) 1926–1940.
- [17] R. L. Amaro, N. Rustagi, K. O. Findley, E. S. Drexler, A. J. Slifka, Modeling the fatigue crack growth of X100 pipeline steel in gaseous hydrogen, *Int. J. Fatigue* 59 (2014) 262-271.
- [18] C. Colombo, G. Fumagalli, F. Bolzoni, G. Gobbi, L. Vergani. Fatigue behaviour of hydrogen pre-charged low alloy Cr-Mo steel. *Int. J. Fatigue* 83 (2016) 2-9.
- [19] J. Yamabe, H. Itoga, T. Awane, H. Matsunaga, S. Hamada and S. Matsuoka, Fatigue-life and leak-before-break assessments of Cr-Mo steel pressure vessels with high-pressure gaseous hydrogen, ASME 2014 Pressure Vessels and Piping Conference, Volume 6B: Materials and Fabrication, Anaheim, California, USA, July 20–24, 2014
- [20] A. Saxena, K. Nibur and A. Prakash, Applications of fracture mechanics in assessing integrity of hydrogen storage systems”, *Eng. Fract. Mech.* 187 (2018) 368-380.
- [21] J. H. Chuang, L.W. Tsay and C. Chen, Crack growth behaviour of heat-treated 4140 steel in air and gaseous hydrogen, *Int. J. Fatigue* 20 (7) (1998) 531-536.
- [22] V. R. Nagarajan, S. K. Putatunda, Influence of dissolved hydrogen on the fatigue crack growth behaviour of AISI4140 steel, *Int. J. Fatigue* 62 (2014) 236-248.
- [23] L.B. Peral, S. Blasón, A. Zafra, C. Rodríguez, F.J. Belzunce, Effect of hydrogen on fatigue crack growth of quenched and tempered CrMo(V) steels. *MATEC Web of Conferneces* 165, Poitiers (France), 03009, 2018.
- [24] K. Sprichal, J. Berka, J. Burda, M. Falcník, Hydrogen embrittlement and fracture mode of EUROFER 97 ferritic-martensitic steel. *Int. J. Pres. Ves. and Piping* 89 (2012) 42-47.
- [25] Y. Ogawa, H. Matsunaga, J. Yamabe, M. Yoshikawa, S. Matsuoka, Unified evaluation of hydrogen-induced crack growth in fatigue tests and fracture toughness test of carbon steel, *Int. J. Fract.* 103 (2017) 223-233.
- [26] J. H. Liu, L. Wang, Y. Liu, X. Song, J. Luo and D. Yuan, Effects of hydrogen on fracture toughness and fracture behaviour of SA508-III steel, *Mater. Res. Innovations* 18 (4) (2014) 255-259.
- [27] K. A. Nibur, B. P. Somerday, C. S. A. N. Marchi, J. W. Foulk, M. Dadfarnia, and P. Sofronis, The Relationship Between Crack-Tip Strain and Subcritical Cracking Thresholds for Steels in High-Pressure Hydrogen Gas, *Metall. Mater. Trans. A* 44 (2013) 248–269.
- [28] I. M. Robertson, P. Sofronis, A. Nagao, M.L. Martins, S. Wang, D.W. Gross and K.E. Nygren, Hydrogen embrittlement understood, *Metall. Mat. Trans. A* 46(6) (2015) 2323-2341.
- [29] A. Nagao, M. Dadfarnia, B.P. Somerday, P. Sofronis, R.O. Ritchie, Hydrogen-enhanced-plasticity mediated decohesion for hydrogen-induced intergranular and quasi-cleavage fracture of lath martensitic steels, *J. Mech. Phys. Solids* 112 (2018) 403-430.
- [30] G.K. Williamson, W.H. Hall, X-ray line broadening from filed aluminium and wolfram, *Acta Metall.* 1, (1953) 22-31.
- [31] Williamson G.K. and Smallman R.E., Dislocation densities in some annealed and cold-worked metals from measurements on the X-ray debye-sherrer spectrum, *Philos. Mag.* 1(1) (1956) 34-46.

- [32] J.P. Hirtz, Effects of hydrogen on the properties of iron and steel, *Metall. Trans. A.* 11 (1980) 861-890.
- [33] San Marchi C., Somerday B.P. Robinson S.L., Permeability, solubility and diffusivity of hydrogen isotopes in stainless steels at high gas pressures, *Int. J. Hydrogen Energy* 32 (2007) 100-116.
- [34] ASTM E1820, Standard test method for measurement of fracture toughness, *Annual Book of ASTM Standards*, Vol. 03.01, 2015.
- [35] George Krauss, *Steels: Processing, Structure and Performance*, ASM International, 2005.
- [36] Y. Takeda and C. J. McMahon Jr, Strain controlled vs. stress controlled hydrogen induced fracture in a quenched and tempered steel, *Metall. Mater. Trans. A* 12 (1981) 1255–1266.
- [37] A. Nagao, M.L. Martin, M. Dadfarnia, P. Sofronis, I.M. Robertson, The effect of nanosized (Ti,Mo)C precipitates on hydrogen embrittlement of tempered lath martensitic steels, *Acta Mater.* 74 (2014) 244-254.
- [38] R.P. Gangloff and B.P. Sommerday, *Gaseous hydrogen embrittlement of materials in energy technologies*. Woodhead Publishing, 2012.
- [39] R.M. McMeeking, D.M. Parks, On criteria for J-dominance of crack-tip fields in large-scale yielding, *ASTM STP 668*, American Society for Testing and Materials, Philadelphia, 1979, 175-194.
- [40] P. Sofronis, R.M. McMeeking, Numerical analysis of hydrogen transport near a blunting crack tip, *J. Mech. Phys. Solids* 37 (1989) 317-350.
- [41] Oriani R. A., The diffusion and trapping of hydrogen in steel, *Acta Metall.* 18 (1970) 147-157.